Mechanistic Insights into N_2O Formation as a Side Product in NH_3-SCR over Small Pore Cu-Zeolites

Yilin Wang [a], *Wenru Zhao* [b], *Yiqing Wu* [a], *Eric D. Walter* [a], *Kenneth G. Rappé* [a,*], *Yong Wang* [a,c], *Suk Bong Hong* [d], *Donghai Mei* [b,*], *Feng Gao* [a,*]

[a] Institute for Integrated Catalysis, Pacific Northwest National Laboratory, P.O. Box 999, Richland, Washington 99354, USA.

[b] School of Materials Science and Engineering, Tiangong University, Tianjin 300387, China.

[c] Voiland School of Chemical Engineering and Bioengineering, Washington State University, Pullman, Washington 99163, USA.

[d] Center for Ordered Nanoporous Materials Synthesis, Division of Environmental Science and Engineering, POSTECH, Pohang 37673, Republic of Korea.

[*] Corresponding authors: ken.rappe@pnnl.gov (KGR); feng.gao@pnnl.gov (FG); dhmei@tiangong.edu.cn (DM).

ABSTRACT

The present contribution provides clarity to N_2O formation mechanisms and key influencing factors during low temperature NH_3-SCR, with the goal of enabling the rational design of advanced SCR catalysts with low greenhouse gas impact. By studying more than 50 small pore Cu-exchanged zeolite SCR catalyst samples, including model catalysts synthesized in our laboratories and state-of-the-art industrial catalysts, we explored a wide range of factors affecting N_2O formation. These factors included Cu loading, support Si/Al ratio, support topology, catalyst aging, reaction temperature and reactant feed composition effects. We probed N_2O formation under both steady-state SCR, and during NH_4NO_3 decomposition via temperature programmed desorption (TPD). Finally, we used DFT to probe energetics of possible N_2O formation pathways. Based on these studies, we confirm that low temperature N_2O formation occurs via multiple reaction pathways that all involve NH_4NO_3 and are supported by Cu moieties that facilitate in-situ NO oxidation to NO_2.

KEYWORDS: NH_3-SCR, N_2O, reaction mechanism, catalyst design, emission control

1. INTRODUCTION

For more than a decade, the ammonia selective catalytic reduction (NH_3-SCR) technique has been widely employed to eliminate oxides of nitrogen (i.e., NOx) from the exhaust of lean-burn engines. This success is due mainly to the development of Cu-exchanged small pore zeolite catalyst Cu/SSZ-13 (a.k.a. Cu/CHA) that provides high NOx reduction activity, high N_2 selectivity, and superior durability versus its predecessors.[1-3] Despite high performance, N_2O inevitably forms as a byproduct during NH_3-SCR over Cu/CHA[4], and understanding N_2O formation mechanisms is highly important for enabling the rational design of SCR catalysts with low N_2O selectivity.

Over Cu-zeolites, N_2O formation during standard NH_3-SCR (R1) follows strong temperature dependence. At low temperature, N_2O formation peaks at 200-250 °C, followed by a dip and increase again at >350 °C.[5] Whereas N_2O formation above 350 °C may originate from both non-selective NOx reduction (R2) and NH_3 oxidation by O_2 (R3), that below ~350 °C is due predominantly to R2, if not entirely, keeping in mind that this is a global stoichiometry for the reaction.[5, 6]

$$4NO + 4NH_3 + O_2 \rightarrow 4N_2 + 6H_2O \quad \text{R1}$$

$$4NO + 4NH_3 + 3O_2 \rightarrow 4N_2O + 6H_2O \quad \text{R2}$$

$$2NH_3 + 2O_2 \rightarrow N_2O + 3H_2O \quad \text{R3}$$

The mechanism for low-temperature N_2O formation remains highly debated. The traditional wisdom, largely adopted from prior research on V_2O_5/TiO_2, states that N_2O originates from NH_4NO_3 decomposition, and NH_4NO_3 forms when NO_2 is present in the reactant feed (R4 + R5).[7-9] More specifically, NO_2 disproportionation (R6) has been suggested to be imperative for the formation of nitrate which further reacts to NH_3 to form NH_4NO_3.[9]

$$2NO_2 + 2NH_3 \rightarrow NH_4NO_3 + N_2 + H_2O \quad \text{R4}$$

$$NH_4NO_3 \rightarrow N_2O + 2H_2O \quad \text{R5}$$

$$2NO_2 + H_2O \rightarrow HNO_3 + HONO \quad \text{R6}$$

How N_2O forms in the absence of gas phase NO_2 is at the center of the debate over Cu-zeolite SCR catalysts; note in particular that unlike V_2O_5/TiO_2, isolated Cu-ions have been suggested to be rather inert in catalyzing NO oxidation to NO_2.[10-12] Therefore, key open questions that need elucidation are: (i) if N_2O formation is due to NH_4NO_3 decomposition, then how does NH_4NO_3 form in the absence of gas phase NO_2? and (ii) if N_2O formation is irrelevant to NH_4NO_3, then what intermediates are responsible for its formation? Next, relevant recent literature reports are summarized.

Chen et al.[5] compared N_2O formation on a small pore Cu/CHA and a large pore Cu/BEA, and they concluded that N_2O formation is due to NH_4NO_3 decomposition, and "surface nitrates" that form via NO oxidation are required for NH_4NO_3 formation. The authors also discovered that N_2O yield is governed by NH_4NO_3 stability, and higher N_2O formation on Cu/BEA is due to lower stability of NH_4NO_3 on this catalyst. Han et al.[13] compared N_2O formation on Cu/CHA, Cu/MFI, and Cu/BEA and concluded that, in addition to N_2O originating from NH_4NO_3 decomposition, there are differences in the stability of NH_4NO_3 on different catalysts. They similarly proposed that the lower N_2O formation on Cu/CHA is due to the CHA support stabilizing NH_4NO_3 deposits. Both studies also suggest that reaction R7, i.e., NH_4NO_3 interacting with NO to form highly unstable NH_4NO_2 that readily decomposes to N_2 and H_2O, is highly important to increasing SCR selectivity to N_2.

$$NH_4NO_3 + NO \rightarrow NH_4NO_2 + NO_2 \rightarrow N_2 + 2H_2O + NO_2 \qquad \text{R7}$$

From the mechanism proposals shown above, NH_4NO_3 can serve both as an SCR intermediate (e.g., R7) and a side reaction intermediate (e.g., R5), and competition between these two reactions determines SCR selectivity. Note that over Cu-zeolites, selectivity toward R7 is typically much higher than that toward R5; for example, by deliberately introducing NH_4NO_3 to the SCR feed, R7 has been practically applied to enhance low temperate deNOx efficiency.[14] Zhang and Yang,[15] Liu et al.,[16] Yao et al.[17] also proposed that N_2O formation during low temperature SCR is due to NH_4NO_3 decomposition. Furthermore, both Liu et al.,[16] and Yao et al.[17] suggested that $Cu(OH)^+$ species promote NH_4NO_3 formation during SCR, for example, by oxidizing SCR intermediate NH_4NO_2 to NH_4NO_3.[17] In addition to NH_4NO_3, an NH_4NO_3-like intermediate, Cu-NO_3[NH_3], has also been proposed to be an important species for N_2O formation;[18, 19] Importantly, kinetic

simulations suggest that (1) Cu-NO_3[NH_3] is more thermally stable than NH_4NO_3 and is likely responsible for N_2O formation at elevated temperatures, and (2) NH_4NO_3 can form via interaction between Cu-[NO_3][NH_3] and H_2O. These two reactions are described below as R8 and R9, where "Z" represents the zeolite support.

$$\text{Z-Cu-}[NO_3][NH_3] \rightarrow \text{Z-CuOH} + N_2O + H_2O \qquad \text{R8}$$

$$\text{Z-Cu-}[NO_3][NH_3] + H_2O \rightarrow \text{Z-CuOH} + NH_4NO_3 \qquad \text{R9}$$

Recently, Negahdar et al.[20] proposed another NH_4NO_3-like intermediate, [SSZ-13((Cu^+)-NH_3)HNO_3], that is responsible for N_2O formation. However, some researchers recently proposed that NH_4NO_3 (or nitrates in general) is irrelevant to N_2O formation during low temperature NH_3-SCR, and three examples of this are described here. First, on the basis of density functional theory (DFT) calculations, Feng et al.[21] proposed a N_2O formation mechanism involving proton transfer from a SCR intermediate H_2NNO to Cu-OOH-Cu complexes, which displays lower activation barriers than that of NH_4NO_3 decomposition [thermally or catalyzed by zeolite Brønsted acid sites (BAS)]. Second, Shih et al.[6] proposed that N_2O forms during the reduction half-cycle of standard SCR involving NH_3-solvated Cu-NH_3NO intermediates aided by oxygen donors (zeolite lattice O, H_2O, or O_2). This mechanism is based mainly on their observation that N_2O formation apparent activation energies are indistinguishable from the standard SCR apparent activation energies. Third, Xi et al.[22] proposed that N_2O forms on Cu-oxy species (e.g., [Cu-O_2-Cu]$^{2+}$) during SCR and, based on the undetectability of nitrate bands via in situ DRIFTS, they excluded the involvement of surface nitrate (or NH_4NO_3) in N_2O formation at 200 °C. We note that the three proposed mechanisms described above, though different in nature, suggest that N_2O forms on SCR active Cu species. In contrast, Negahdar et al.[20] proposed that N_2O does not form on SCR active Cu but rather on linear copper species such as $CuAlO_2$. Therefore, discrepancies in the pathway of N_2O formation persist, warranting further investigation.

The present contribution intends to provide clarity to N_2O formation mechanisms during low temperature NH_3-SCR. We limit ourselves to small pore Cu-exchanged SCR catalysts including Cu/SSZ-13 (Cu/CHA), Cu/SAPO-34, Cu/SSZ-39 (Cu/AEI) and Cu/LTA. By examining over 50 catalyst samples - including model catalysts synthesized in our laboratories and state-of-the-art industrial catalysts - we systematically explored a broad range of factors influencing N_2O

formation. These factors include Cu loading, support Si/Al ratio, support topology, catalyst aging, reaction temperature, and reactant feed composition effects. We probed N_2O formation under both steady-state SCR and during NH_4NO_3 decomposition via temperature programmed desorption (TPD). Finally, we used DFT to probe energetics of possible N_2O formation pathways. Collectively, the results presented here demonstrate that low temperature N_2O formation occurs via multiple reaction pathways, all of which that must involve NH_4NO_3, supported by Cu moieties that facilitate in-situ NO oxidation to NO_2[12] and subsequent NH_4NO_3 formation via interaction with NH_3.

2. METHODS

2.1. Catalyst Preparation and Treatments.

More than 50 Cu catalysts were used in the present study, and the abbreviated names, sources, synthesis methods, compositions and post-synthesis treatments of the catalyst are tabulated in **Table S1**. More details on synthesis (both zeolite supports and Cu-exchanged catalysts) and routine characterizations on physicochemical properties are summarized in **Note S1**. The catalysts studied include (Group 1) fresh Cu/CHA with varying Cu loading from aqueous ion exchange (AIE) and constant Si/Al = 6.7;[23] (Group 2) fresh Cu/CHA with varying Si/Al and constant Cu loading from AIE;[12] (Group 3) fresh Cu/CHA with varying Si/Al and constant Cu loading from solid-state ion exchange (SSIE);[12] (Group 4) industrial Cu/CHA catalysts (Cu~2.5 wt.%, Si/Al~12) provided by Cummins, Inc. with varying aging treatment and/or on-road application history;[24] (Group 5 & 6) fresh & hydrothermally aged (HTA) Cu/CHA, Cu/AEI and Cu/LTA for topology effect comparisons, formed via AIE and SSIE;[25] (Group 7 & 8) Cu/SAPO-34 from Zeolyst, Inc., and Cu/SAPO-34 synthesized in-house via a one-pot method or via SSIE. Two more AIE samples (Group 9 & 10) were specifically prepared, and their purposes will be described as they first appear in the context.

2.2. Steady-State SCR Testing and Data Analysis.

Steady-state NH_3-SCR was measured in a plug-flow reactor system described earlier.[26, 27] Typically, 120 mg of sieved Cu catalyst or the H-form zeolite support (60–80 mesh) was used for the reaction tests. The gas feed consisted of 350 ppm NH_3, 350 ppm NOx (NO_2/NOx ~ 0.03, 0.25, 0.50, 0.75), 10% O_2, 2.5% H_2O (when used), and balance N_2. The total flow rate was 10 mL s^{-1}

and the gas hourly space velocity (GHSV) was estimated to be ~2×10^5 h^{-1}. Concentrations of reactants and products were measured by an MKS MultiGas 2030 FTIR gas analyzer with the gas cell held at 191 °C. Reactions were carried out in two manners: temperature-dependent measurements (100-550 °C) at fixed NO_2/NOx ratios, and NO_2/NOx ratio-dependent measurements at fixed temperatures. The following equations were used to calculate NOx and NH_3 conversions.

$$\mathrm{NO_x\ Conversion\ \%} = \frac{(\mathrm{NO+NO_2})_{\mathrm{inlet}} - (\mathrm{NO+NO_2+N_2O})_{\mathrm{outlet}}}{(\mathrm{NO+NO_2})_{\mathrm{inlet}}} \times 100$$

$$\mathrm{NH_3\ Conversion\ \%} = \frac{(\mathrm{NH_3})_{\mathrm{inlet}} - (\mathrm{NH_3})_{\mathrm{outlet}}}{(\mathrm{NH_3})_{\mathrm{inlet}}} \times 100$$

We note that most SCR reaction data described here were acquired using a diluted NO gas tank that we determined was slightly contaminated with NO_2 (NO_2/NOx ~ 0.03). However, this contamination had little influence on N_2O formation during our standard SCR tests. We confirmed this by comparing a sub-set of results to that using another cylinder of dilute NO with much less contamination (NO_2/NOx ~ 0.004) and yielding highly reproducible N_2O formation data.

Standard SCR rate constant *k* was calculated using a first-order kinetic equation $k = \frac{r}{[NOx]_0} = \frac{F}{W[NOx]_0}(-\ln(1-x))$, where *r* is the reaction rate (moles of NOx g_{cat}^{-1} s^{-1}), $[NOx]_0$ the inlet concentration, *F* the NOx flow rate (moles of NOx s^{-1}), *W* the mass of the catalyst (g), and *x* the NOx conversion.[28] Following which, Arrhenius analysis was carried out by plotting Ln(k) vs. 1/T, where the low temperature linear regime data were used to derive SCR apparent activation energies $E_{a,\,SCR}$. N_2O formation apparent activation energies, on the other hand, were derived by plotting Ln(N_2O outlet concentration) vs. 1/T. Again, the low temperature linear regime data were used to calculate N_2O formation apparent activation energies $E_{a,\,N_2O}$.[6] Note that N_2O concentrations are always much lower than NO inlet concentrations; as such, under reaction conditions where SCR is under kinetic control, it is reasonable to assume that N_2O formation is also under kinetic control. The Koros-Nowak criterion has been applied to rule out mass transfer limitations, and this has also been demonstrated in prior work.[27] For temperature-dependent measurements conducted at higher NO_2/NOx ratios, and for NO_2/NOx ratio-dependent measurements carried out at fixed temperatures, N_2O concentrations were reported directly without further data analysis.

2.3. Temperature Programmed Desorption (TPD) Analysis.

TPD analyses were conducted on catalysts containing NH_4NO_3 deposits. Two methods were used to introduce NH_4NO_3 to the Cu-SCR catalysts and the H-form zeolite supports: (i) impregnation with NH_4NO_3 aqueous solution, and (ii) in situ NH_4NO_3 deposition under "fast SCR" (R10) at 100 °C.

$$NO + NO_2 + 2NH_3 \rightarrow 2N_2 + 3H_2O \qquad R10$$

For the former, NH_4NO_3 was dissolved in deionized H_2O, and incipient wetness impregnation was used to add NH_4NO_3 to the zeolite (~0.6 ml solution / g of zeolite). The sample was subsequently dried at room temperature, and the resulting solid was used in the TPD experiment. For the latter, the zeolite was exposed to fast SCR reaction at 100 °C which occurs almost exclusively as R4 (described above),[29] allowing NH_4NO_3 deposition to occur inside the zeolite pores, and the reaction was stopped when outlet NOx and NH_3 concentrations became invariant with time. TPD experiments were conducted by first purging with N_2 for 1 h at ambient temperature and then ramping the temperature to 550 °C at 3 °C min^{-1}, with gaseous products recorded using the FTIR gas analyzer described above.

2.4. Density Functional Theory (DFT) Calculations.

The periodic DFT calculations were conducted using the QUICKSTEP module within the CP2K software package.[30, 31] The exchange-correlation functional employed was the Perdew, Burke, and Enzerhof (PBE) generalized gradient approximation (GGA) with mixed Gaussian and plane-wave basis sets.[32] Core electron wavefunctions were represented using norm-conserving Goedecker-Teter-Hutter pseudopotentials,[33] while valence electron wavefunctions were extended in a double zeta basis set with polarization functions and an auxiliary plane wave basis set.[34] A kinetic energy cutoff of 360 Ry and an SCF convergence criteria of 1.0×10^{-8} arbitrary units were utilized. Test calculations demonstrated that a maximum force convergence criterion smaller than 0.001 Hartree/Bohr resulted in a negligible total energy change of the system (< 0.01 eV). All structural optimizations were carried out using the Broyden-Fletcher-Goldfarb-Shanno (BGFS) algorithm. Additionally, to account for van der Waals (vdW) interactions, the DFT-D3 correction developed by Grimme et al.[35] was included in all calculations. In this study, we employed the climbing image elastic band (CI-NEB) method[36, 37] to ascertain the transition states of each elementary reaction step involved in the NH_3-SCR reaction leading to N_2O formation in the

Cu/CHA zeolite catalyst. By utilizing seven (7) intermediate images along the reaction pathway between the initial and final states, we were able to pinpoint the transition state for each step. Furthermore, the validity of each identified transition state was confirmed through vibrational frequency analysis, which revealed the presence of only one imaginary frequency at the transition state.[38] Gibbs free energy of reaction (ΔG) and Gibbs free energy of activation ($\Delta G^{\ddagger}$) were calculated using the standard statistical thermodynamics methods.[39-41]

The periodic CHA zeolite model was prepared using two hexagonal unit cells with the size parameters of 13.6750 × 23.6858 × 14.7670 $Å^3$. Since commercial Cu/CHA catalysts typically have support Si/Al ratios of ~12,[42] herein this composition was adopted by replacing 6 Si atoms on the CHA framework with 6 Al atoms, and compensating the charges with additional 6 H atoms on the O atoms, resulting in the model CHA zeolite of $H_6Al_6Si_{66}O_{144}$ with the Si/Al of 11.[43-46] In particular, two Al atoms at the eight-membered ring (8MR) between the two CHA cages were assigned, resulting in two Brønsted acid sites (BAS) at the 8MR.

3. RESULTS

3.1. $E_{a,\,SCR}$ and $E_{a,\,N_2O}$ Comparison.

NH_4NO_3 forms with high stability on SCR catalysts and is arguably more stable than other possible intermediates involved in low-temperature SCR.[5, 13] Thus, it can be inferred that if N_2O originates from NH_4NO_3 decomposition, then $E_{a,\,N_2O}$ can be greater than $E_{a,\,SCR}$, whereas if N_2O originates from some unstable SCR intermediates other than NH_4NO_3, then $E_{a,\,N_2O}$ may be less than $E_{a,\,SCR}$. This forms the key hypothesis for this work. Based on this, first we present a considerable body of work to obtain $E_{a,\,SCR}$ and $E_{a,\,N_2O}$ during low temperature standard SCR, and to clarify the likelihood of NH_4NO_3 involvement in N_2O formation. Next, using the group of Cu/CHA catalysts with Si/Al = 6.7 and varying Cu loadings as an example,[23] we show how $E_{a,\,N_2O}$ and $E_{a,\,SCR}$ values are acquired and compared.

Figure S1 presents NOx conversion and N_2O formation data (in ppm) as a function of reaction temperature for the Group 1 catalysts (fresh Cu/CHA, Si/Al = 6.7, AIE prepared, varying Cu loading). Using these data and the Arrhenius analysis protocols described above, **Figures 1a, 1b** present Arrhenius plots that are used to derive $E_{a,\,SCR}$ and $E_{a,\,N_2O}$, respectively, and **Figure 1c**

depicts their comparison. For this group of catalysts, with the exception of Cu/CHA-7-1 $E_{a,\ N_2O}$, both $E_{a,\ SCR}$ and $E_{a,\ N_2O}$ increase with increasing Cu loading, and $E_{a,\ N_2O}$ are consistently ~10-20 kJ/mol lower than the corresponding $E_{a,\ SCR}$. This result suggests that N_2O originates from highly unstable intermediates other than NH_4NO_3, or facile NH_4NO_3 catalytic decomposition reactions occur.

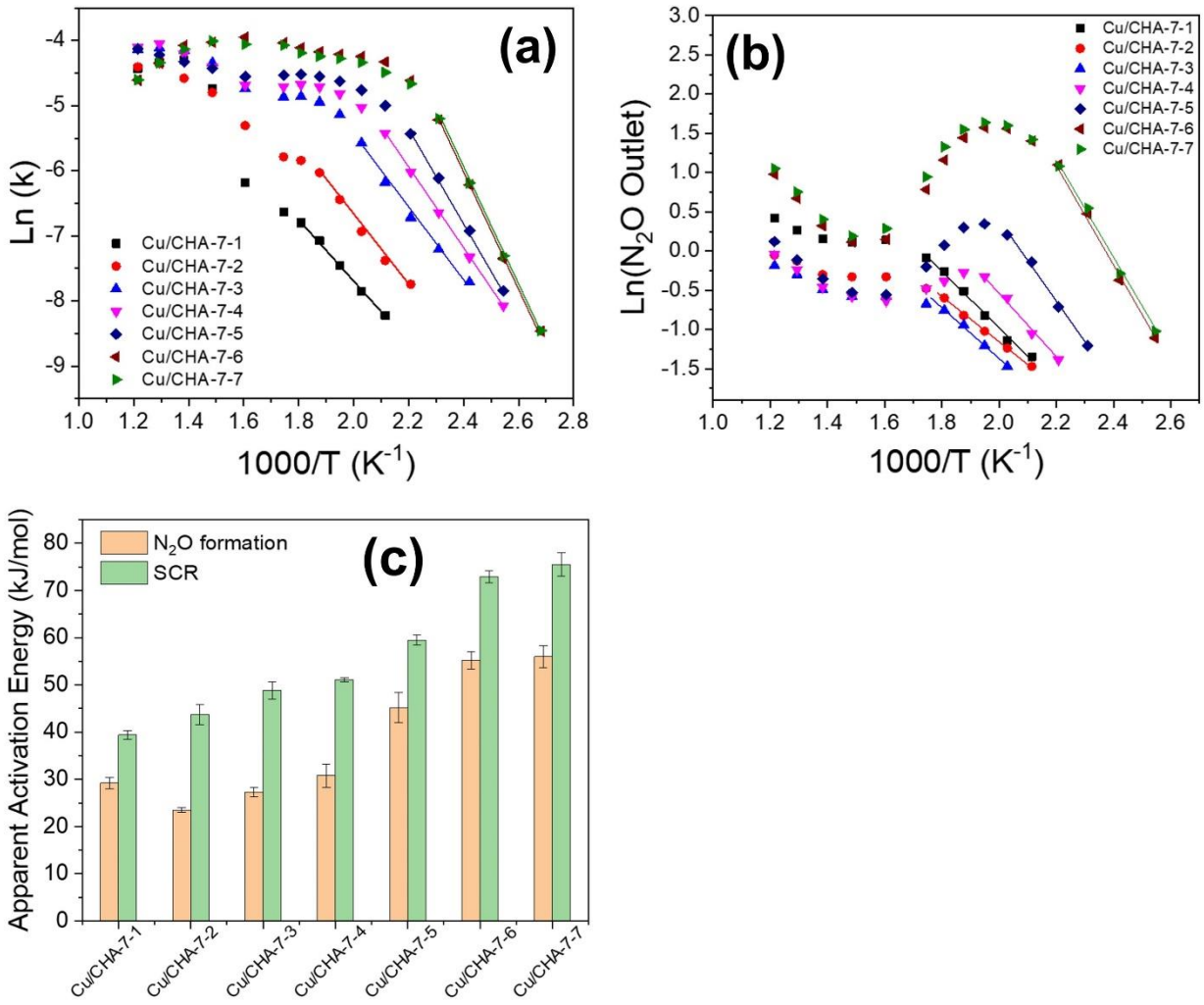

Figure 1. Standard SCR over the Si/Al = 6.7 series of Cu/CHA catalysts. (a) Ln(k) vs. 1/T Arrhenius plots; (b) Ln(N_2O outlet) vs. 1/T Arrhenius plots; (c) comparative bar plots between $E_{a,\ SCR}$ (green) and $E_{a,\ N_2O}$ (orange) derived from (a) and (b). Error bars in (c) denote standard deviation of linear regression in Arrhenius analysis.

Furthermore, it can be ruled out that N_2 and N_2O share the same rate-determining intermediate decomposition pathway. This is because, if they did, then the lower $E_{a,\,N_2O}$ would display a higher rate, yet N_2O formation rates are much lower than N_2. Also note that at low Cu loadings, N_2O formation rates are not positively correlated with Cu loading. For example, Cu/CHA-7-3 displays lower N_2O formation rates than Cu/CHA-7-1, yet the former contains >3x the total & isolated Cu content than the latter. For the other catalyst groups included in **Table S1**, the same data analysis was carried out. For the sake of simplicity, the results are only shown in the SI as **Figure S2-S8.**

Figure 2 depicts $E_{a,\,SCR}$ versus $E_{a,\,N_2O}$ plots for all groups of catalysts, distinguished by labels of different shapes and colors. To guide the eye, a solid line representing $E_{a,\,SCR} = E_{a,\,N_2O}$ and two dashed lines representing $E_{a,\,SCR} = E_{a,\,N_2O} \pm 20$ kJ/mol are also included. A few salient points are worth noting for these data, as follows:

1. Cu/CHA, Cu/AEI and Cu/LTA catalysts synthesized via AIE, particularly fresh samples with relatively low Si/Al ratios (≤ 15), display $E_{a,\,N_2O}$ values consistently ~20 kJ/mol less than $E_{a,\,SCR}$.

2. Cu/SAPO-34 catalysts, except those synthesized via SSIE, display $E_{a,\,N_2O}$ values consistently less than $E_{a,\,SCR}$ by >20 kJ/mol.

3. Fresh Cu/CHA catalysts with high Si/Al ratios (≥ 18) synthesized via AIE display $E_{a,\,N_2O}$ values considerably greater (up to >40 kJ/mol) than $E_{a,\,SCR}$.

4. Most Cu/CHA, Cu/AEI and Cu/LTA catalysts synthesized via SSIE display $E_{a,\,N_2O}$ values greater than $E_{a,\,SCR}$ by up to > 20 kJ/mol.

5. High milage industrial Cu/CHA catalysts (with sulfur contamination) display $E_{a,\,N_2O}$ values slightly greater than $E_{a,\,SCR}$.

6. Hydrothermal aging induces complex effects to N_2O formation that do not appear to display a clear trend.

From the results shown in **Figure 2**, it is clear that low temperature N_2O formation cannot be explained by one mechanism that applies to all catalysts. Where $E_{a,\,N_2O} < E_{a,\,SCR}$ (e.g., Group 1,

Cu/CHA Si/Al = 6.7), N_2O could originate from highly unstable intermediates as previously suggested by Feng et al.[21]. However, where $E_{a,\,N_2O} > E_{a,\,SCR}$, including $E_{a,\,N_2O}$ as high as ~95 kJ/mol (i.e., higher than most $E_{a,\,SCR}$ ever reported in literature for standard SCR), the involvement of NH_4NO_3 (or nitrate in general) in N_2O formation cannot be ruled out. Since multiple N_2O formation mechanisms are likely reflected in the N_2O formation rates, we compare standard SCR and N_2O formation rates at low temperatures.

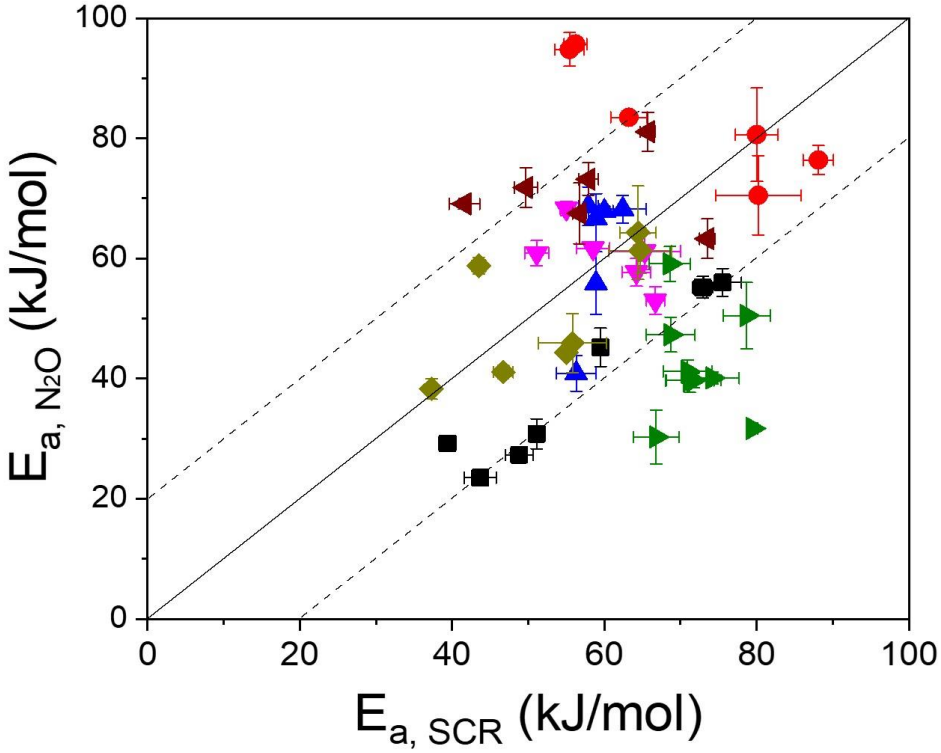

Figure 2. $E_{a,\,SCR}$ versus $E_{a,\,N_2O}$ plots for the 7 groups of catalysts. (■) fresh AIE Cu/CHA with Si/Al = 6.7; (●) fresh AIE Cu/CHA with varying Si/Al ratios from 12 to 36; (▲) fresh SSIE Cu/CHA with varying Si/Al ratios from 6 to 36; (▼) high milage commercial Cu/CHA acquired from Cummins, Inc.; (♦) fresh and hydrothermally aged (850 °C) AIE Cu/CHA, Cu/AIE and Cu/LTA; (◄) fresh SSIE Cu/CHA, Cu/AIE, Cu/LTA and Cu/SAPO-34; (►) fresh and hydrothermally treated Cu/SAPO-34 acquired from Zeolyst, Inc. and synthesized in-house via a one-pot method.

3.2. Standard SCR and N_2O Formation Rate Comparisons.

The ratios of N_2O formation rates to standard SCR rates ($\frac{r_{N_2O}}{r_{SCR}}$) at 160 °C are plotted in **Figure 3** as a function of $E_{a,\,SCR}$. This temperature is low enough so that both SCR and N_2O formation are confidently under rigorous kinetic control (i.e., within the low-temperature linear Arrhenius regime). Over (i) fresh Cu/CHA, Cu/AEI and Cu/LTA synthesized via AIE and (ii) some of the fresh SSIE catalysts with relatively low Si/Al ratios (i.e., samples that contain negligible CuO, marked by the shaded area), $\frac{r_{N_2O}}{r_{SCR}}$ displays an exponential correlation with $E_{a,\,SCR}$ (**Figure S9**). Prior studies have demonstrated clearly that low temperature standard SCR follows a redox mechanism involving reduction ($Cu^{II} \rightarrow Cu^{I}$) and oxidation ($Cu^{I} \rightarrow Cu^{II}$) half cycles. It has also been repeatedly reported that increased Cu-ion loading typically leads to $E_{a,\,SCR}$ increase from increased rate-control by the reduction half cycle.[23, 27, 47] Regarding speciation of two types of SCR active Cu-ions in Cu/CHA, i.e., Z_2Cu^{II} and $ZCu^{II}OH$, prior studies have shown that the thermodynamically stabler Z_2Cu^{II} tend to populate first, followed by population of less stable (and thus more reactive) $ZCu^{II}OH$ as Cu loading increases.[23, 48] As such, the positive correlation between $E_{a,\,SCR}$ and N_2O yield on these "CuO free" samples appears consistent with the proposal by Shih et al.[6] that N_2O forms on $ZCu^{II}OH$ sites. However, for samples with non-negligible CuO content (e.g., most Cu/CHA, Cu/AEI and Cu/LTA samples formed via SSIE, and/or aged samples), $\frac{r_{N_2O}}{r_{SCR}}$ can become ~4 times higher than that of the "CuO free" samples at similar $E_{a,\,SCR}$ values. Most of the Cu/SAPO-34 catalysts, in contrast, display $\frac{r_{N_2O}}{r_{SCR}}$ lower than the "CuO free" Cu-zeolite samples. In short, results shown in **Figure 3** show that N_2O formation positively correlates with increased Cu-ion content and is promoted by CuO, and SAPO-34 displays a unique inhibitory effort toward N_2O formation.

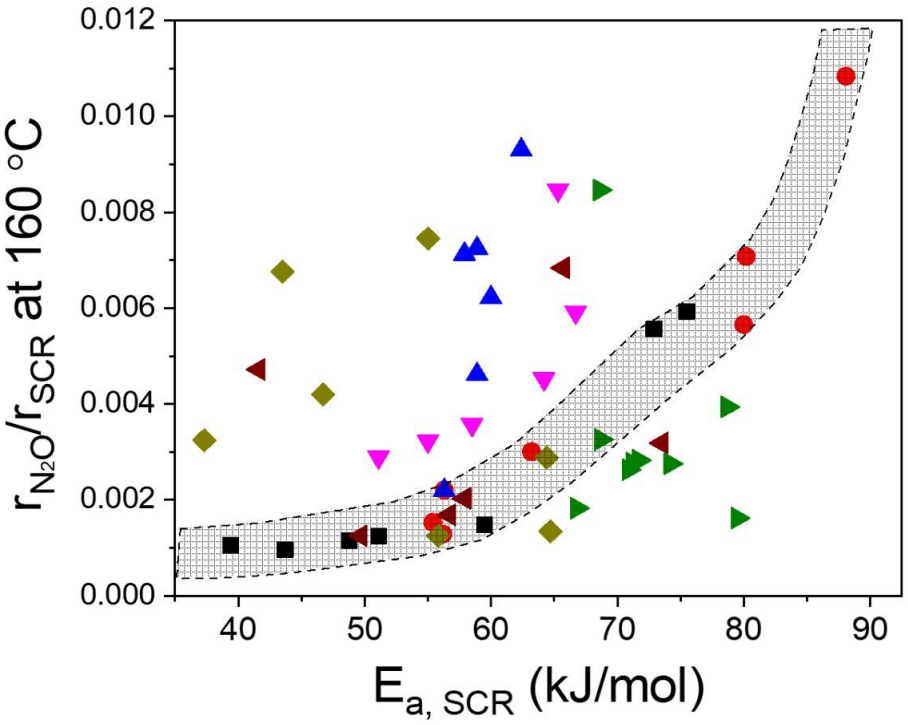

Figure 3. $E_{a,\ SCR}$ versus $\frac{r_{N_2O}}{r_{SCR}}$ plots for the 7 groups of catalysts at a reaction temperature of 160 °C. Sample labels are the same as those in **Figure 2**. The shaded area incorporates mainly fresh AIE Cu/CHA, Cu/AEI, Cu/LTA and SSIE samples containing minimal CuO.

3.3. "In situ" NO_2 Effects on N_2O Formation.

Multinuclear Cu_xO_y species, and CuO in particular, are known to catalyze both NO (R11) and NH_3 oxidation (R12). N_2O is not a side product of NO oxidation over Cu-zeolites[10, 12, 49], however, NH_3 oxidation over Cu-zeolites does generate small amounts of N_2O.[12, 50] Since non-selective NH_3 oxidation over Cu-zeolites typically lights-off >200 °C, it is unlikely that N_2O formed at low temperatures (e.g., 160 °C) during SCR derives from this. As such, the additional N_2O formed on CuO-containing samples (**Figure 3**) is likely due to NO oxidation to NO_2 (catalyzed by CuO) that subsequently enables NH_4NO_3 formation & decomposition, e.g., as described by R4+R5.

$$2NO + O_2 \rightarrow 2NO_2 \qquad \text{R11}$$

$$4NH_3 + 3O_2 \rightarrow 2N_2 + 6H_2O \qquad \text{R12}$$

To corroborate this hypothesis, we compare the standard SCR performance of two Cu/CHA samples with similar low isolated Cu-ion content: one with negligible CuO (Cu/CHA-36L, Si/Al ~36, 0.54 wt.% isolated Cu-ion via AIE) and one with 0.89 wt.% CuO (Cu/CHA-36s, 0.61 wt.% isolated Cu-ion via SSIE). From the standard SCR NOx light-off plots shown in **Figure S10**, Cu/CHA-36L exhibit poor low-temperature activity due to severe kinetic limitations from the oxidation half cycle due to its low Cu loading.[23, 51] In contrast, Cu/CHA-36s shows drastically higher low-temperature NOx conversion efficiency despite its similar isolated Cu-ion content to Cu/CHA-36L. We attribute the difference to fast SCR (R10) on Cu/CHA-36s that is enabled by "in situ" NO_2 formation via R11 catalyzed by CuO. It should be clarified that, although the ZCuOH and Z_2Cu contents in Cu/CHA-36L were not directly measured, its Cu:Al ratio combined with the predicted Cu site compositional phase diagram versus Si:Al and Cu:Al ratios previously reported allows for the estimation of ~80% of Cu-ions in Cu/CHA-36L stay as CuOH.[48]

Next, we compare N_2O formation on Cu/CHA-36L and Cu/CHA-36s in **Figure 4**, in addition to two other "CuO free" samples, Cu/CHA-12 and Cu/CHA-18. Two important points are worth mentioning regarding this data. First, at low temperatures N_2O formation on Cu/CHA-36L is negligible, and if N_2O only generates during the reduction half-cycle of isolated Cu-ions as suggested by Shih et al.,[6] then N_2O formation on Cu/CHA-36s should also be negligible. This follows from the absence of $Cu^{II} \leftrightarrow Cu^{I}$ redox requirement in fast SCR as evidenced by Cu^{2+} the only Cu oxidation state observed by McEwen et al.[52] However, much more N_2O is generated on Cu/CHA-36s via pathways that are otherwise impossible without invoking NH_4NO_3 (i.e., R11+R4+R5). Second, low temperature N_2O formation over Cu/CHA-12 and Cu/CHA-18 is largely indistinguishable from that over Cu/CHA-36s. This similarity also challenges recent proposals that low temperature N_2O formation is irrelevant to NH_4NO_3, as it is difficult to envision that N_2O formation via very different NH_4NO_3-free mechanisms that would be induced on these catalysts, owing to their unique Cu speciation, follow highly similar kinetics.

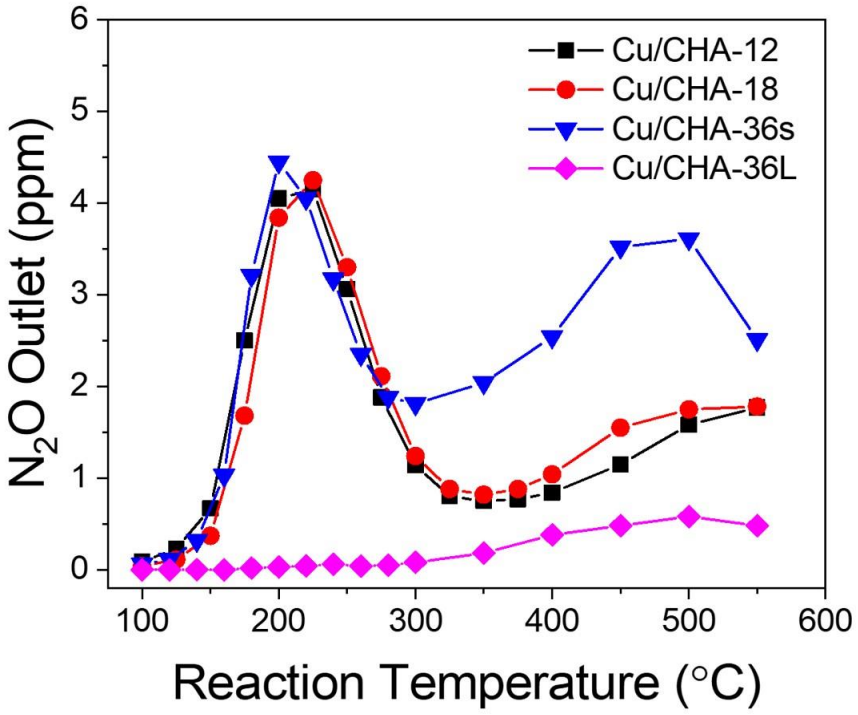

Figure 4. N_2O outlet concentration versus temperature plots for standard SCR on Cu/CHA-36L, Cu/CHA-36s, Cu/CHA-12 and Cu/CHA-18. The reactant feed contains 350 ppm NOx (including ~10 ppm NO_2), 350 ppm NH_3, 2.5% H_2O, 10% O_2, and balanced N_2 at a GHSV of ~2×10^5 h^{-1}.

3.4. Gas Phase NO_2 Effects on N_2O Formation.

N_2O formation was probed during steady-state SCR time-on-stream analysis at varying reactant NO_2/NOx ratios over selected H-form zeolites and SAPO-34 (**Table S2**) and their respective Cu-containing catalyst analogs prepared via SSIE at a common 2.0 wt.% Cu loading. An additional SSIE Cu/SAPO-34 catalyst (Cu/SAPO-bs) containing 1.5 wt.% Cu was also included here. For these tests, 240 °C reaction temperature was used since NH_4NO_3 does not accumulate indefinitely at this temperature precluding steady state.[29] **Figure S11** and **Figure S12** present time-on-stream outlet concentrations of NO, NO_2, N_2O and NH_3 over the H-form supports Cu catalysts, respectively, and **Figure 5a** and **Figure 5b** summarize the N_2O formation results from these tests, respectively. On the H-form samples under low NO_2/NOx of ~0.03, N_2O outlet concentrations are very low (much lower than inlet NO_2 = ~10 ppm) and increasing NO_2/NOx ratio rapidly increases N_2O yields over all samples. This suggests that gaseous NO_2 supply is

indispensable for N_2O formation over the H-form samples and, as such, R4+R5 best describes the N_2O formation pathways. This notion will be further corroborated below by NH_4NO_3 TPD results.

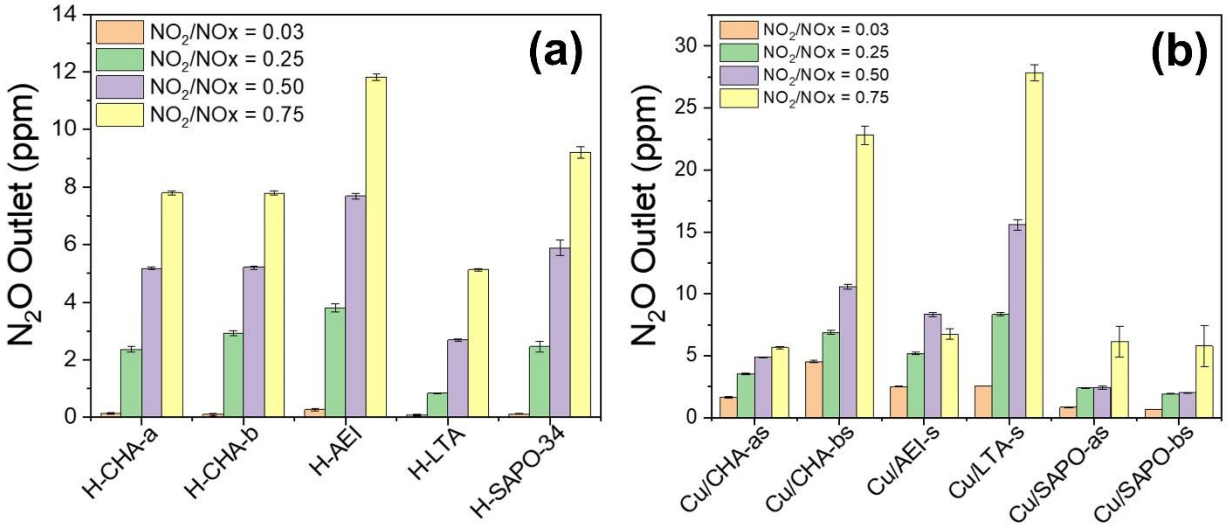

Figure 5. N_2O outlet concentration as a function of NO_2/NOx ratio during steady-state SCR over (a) H-form zeolites and (b) the corresponding Cu catalysts at a reaction temperature of 240 °C. The reactant feed contains 350 ppm NOx, 350 ppm NH_3, 2.5% H_2O, 10% O_2, and balanced N_2 at a GHSV of ~2×10^5 h^{-1}. The 350 ppm NOx consists of the following NO_2 fractions and the remainder NO: NO_2/NOx = 0.03 (orange), 0.25 (green), 0.50 (purple), 0.75 (yellow).

To elucidate possible correlations between N_2O formation and Brønsted acid site (BAS) strength and density of these H-zeolites/H-SAPO-34, NH_3-TPD was carried out to probe their BAS properties, and the results are depicted in **Figure S13**. Based on NH_3 desorption temperatures and peak areas, it is concluded that:

i. H-CHA and H-AEI have stronger Brønsted acidity than H-LTA and H-SAPO-34, and

ii. BAS density follows the trend H-CHA-a ≈ H-SAPO-34 > H-AEI > H-CHA-b ≈ H-LTA, consistent with their composition shown in **Table S2**.

From the results in **Figure S11**, it is clear that higher BAS *density* slows NH_4NO_3 accumulation/poisoning as evidenced by the longer reaction time needed for H-CHA-a and H-SAPO-34 to reach steady state at NO_2/NOx = 0.25; this emphasizes the role of BAS in catalyzing

NH_4NO_3 decomposition. Regarding N_2O yield, the situation is more complex: whereas low N_2O formation over H-LTA may be due to its low BAS strength and/or density, there is not clear correlation between BAS and N_2O yields over the other H-zeolites. For example, though H-CHA-a and H-CHA-b have different BAS density and both have higher BAS strength than H-SAPO-34, these three samples show similar N_2O yields at analogous NO_2/NOx ratios. A likely explanation is that N_2O formation via R5 can proceed both thermally and BAS-catalyzed, and the lack of strong correlation between N_2O yield and BAS at 240 °C suggests that both NH_4NO_3 decomposition pathways exist at this temperature. This notion will be further corroborated in the following.

Regarding the time-on-stream results for the Cu catalysts shown in **Figure S12** and summarized for N_2O in **Figure 5b**, we highlight only key differences between these data and data from the H-form catalysts in **Figure S11** and **Figure 5a**. First, the Cu catalysts take much longer to reach steady state at most reaction conditions (in particular, NO_2/NOx = 0.75 on Cu/SAPO-34) versus the H-form catalysts. This is expected given the relation of NH_3 inventory to Cu-catalyzed SCR, and the fact that NH_3 inventory does not build fast at this temperature. Second, steady state arrives more quickly over catalysts with stronger support BAS strength, i.e., Cu/CHA-as(bs) and Cu/AEI-s, which we attribute to stronger BAS strength building NH_3 inventory more quickly. Third, N_2O typically reaches (quasi) steady state considerably faster than NO_2 and NH_3. This provides further evidence that N_2O production is not intimately linked to Cu-catalyzed SCR processes, and it also indicates different site involvement between NH_4NO_3 formation (affecting the arrival of a steady state) and NH_4NO_3 decomposition (governing N_2O production). Referencing the N_2O formation results in **Figure 5b**, N_2O yields over the Cu catalysts at NO_2/NOx = 0.03 are clearly higher than those over the H-form supports. This is anticipated since both isolated Cu-ions and CuO clusters enable low temperature N_2O formation (**Figure 4**). At higher NO_2/NOx ratios, N_2O yield comparison between the H-form and Cu-form catalysts leads to three scenarios:

i. Cu/CHA-as and Cu/AEI-s generate similar amounts of N_2O as their H-form counterparts,

ii. Cu/CHA-bs and Cu/LTA-s generate more N_2O than their H-form counterparts, and

iii. Cu/SAPO-as(bs) generate less N_2O than H-SAPO-34.

Such diversity points to complex Cu and BAS interplay on NH_4NO_3 formation and decomposition. Over the Cu/CHA-12 catalyst, we also carried out steady-state measurements at varying temperatures (400-100 °C) and NO_2/NOx ratios (0.03-0.50); the N_2O formation plots are depicted in **Figure S14**. At every temperature, N_2O yield increases with increasing NO_2/NOx ratio as expected. It is also interesting that N_2O formation under fast SCR (NO_2/NOx = 0.5) displays two maxima at ~200 and ~280 °C, a phenomenon that is not observed at lower NO_2/NOx ratios. Since NH_4NO_3 involvement on N_2O formation is generally accepted when gaseous NO_2 reactant is present, results from **Figure S14** corroborate experimental observations shown earlier, particularly (1) under circumstances where NH_4NO_3 involvement is affirmative (NO_2/NOx = 0.25) and doubtful (NO_2/NOx = 0.03), N_2O formation profiles can be highly similar; (2) under circumstances where NH_4NO_3 formation is rapid (NO_2/NOx = 0.5), there clearly exist more than one NH_4NO_3 decomposition pathways.

3.5. TPD Studies.

To further disentangle different N_2O formation pathways, herein we use TPD to study NH_4NO_3 decomposition to N_2O on selected H-zeolites and Cu catalysts. Due to the complex nature of NH_4NO_3 decomposition itself,[53] and the fact that certain decomposition products (i.e., N_2 and O_2) cannot be monitored with our FTIR gas analyzer, we focus on the semiquantitative analysis of N_2O formation rather than providing detailed NH_4NO_3 decomposition pathways.

3.5.1. TPD studies of NH_4NO_3 impregnated on H-CHA and Cu/CHA.

A H-SSZ-13 zeolite with Si/Al ~ 12 and a Cu/SSZ-13 catalyst synthesized using this zeolite as support (total Cu loading 2.18 wt.%, isolated Cu-ion content 2.09 wt.%), denoted H-CHA-i and Cu/CHA-i, respectively, were used for TPD studies following NH_4NO_3 impregnation. **Figures 6a, 6b**, and **6c** compare N_2O formation during TPD under various feed conditions with varying amounts of impregnated NH_4NO_3; **Figure 6a** compares H-CHA-i and Cu/CHA-i in 10% O_2/N_2 with 5 wt.% NH_4NO_3, **Figure 6b** shows Cu/CHA-i with 0.6 – 10.0 wt.% NH_4NO_3 in 10% O_2/N_2, and **Figure 6c** shows Cu/CHA-I under differing feed conditions.

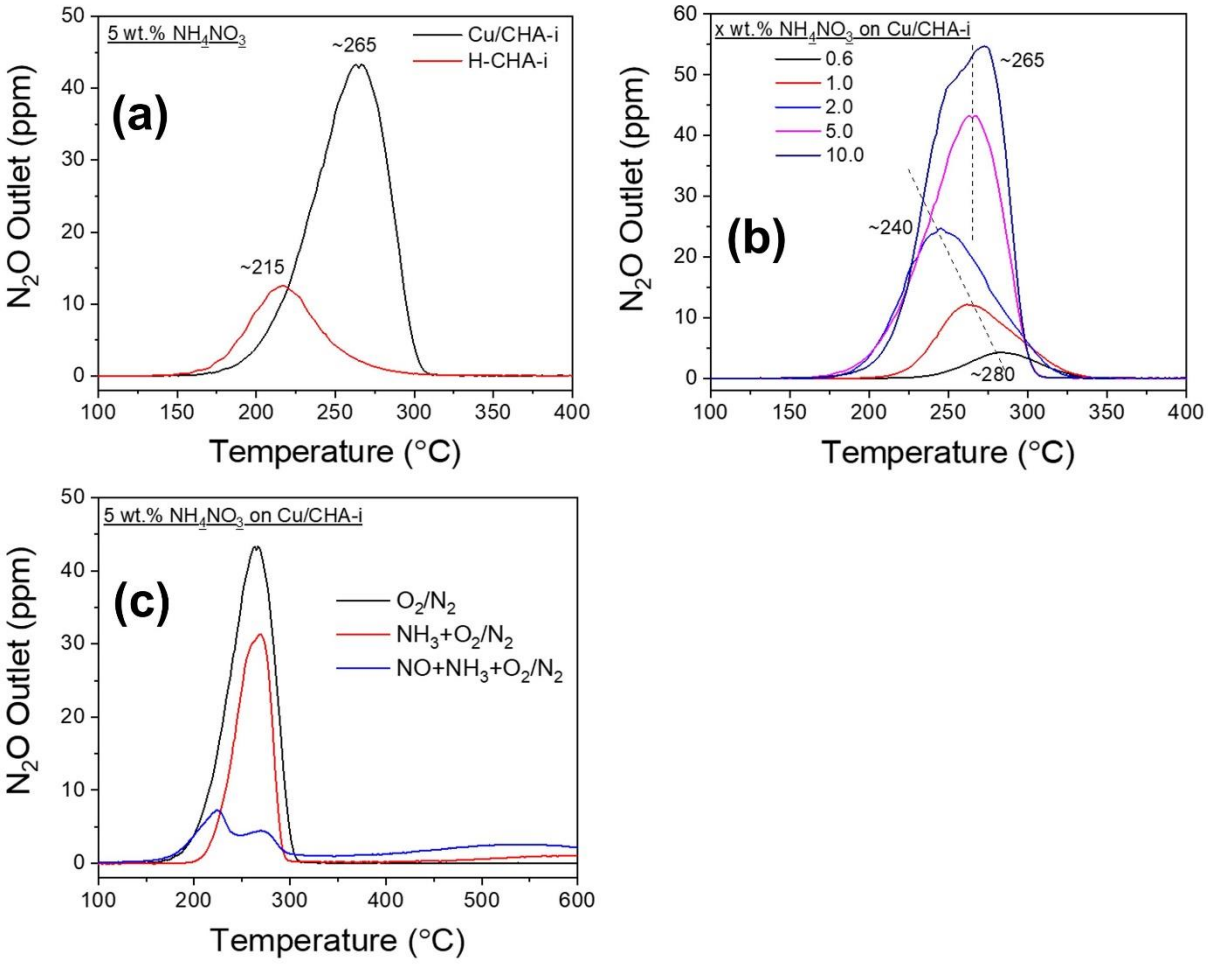

Figure 6. N_2O outlet concentration as a function of temperature in temperature-programmed desorption (TPD) following NH_4NO_3 impregnation. (a) 5 wt.% NH_4NO_3 on H-CHA-i and Cu/CHA-i, in 10% O_2/N_2 flow; (b) 0.6-10.0 wt.% NH_4NO_3 on Cu/CHA-i, in 10% O_2/N_2 flow; (c) 5.0 wt.% NH_4NO_3 on Cu/CHA-i, in 10% O_2/N_2, 350 ppm NH_3 + 10% O_2/N_2, and 350 ppm NH_3 +350 ppm NO + 10% O_2/N_2 flows. 120 mg catalyst, gas flow 600 ml/min, ramping rate 3 °C/min.

On H-CHA-i in **Figure 6a**, a symmetric N_2O peak at ~215 °C is observed; on Cu/CHA-i, N_2O evolution shifts to higher temperature (~265 °C) and its peak becomes asymmetric with a lower temperature shoulder. Because of the chemical inertness of N_2O, both N_2O features are evolved products of reaction/decomposition and not desorption limited. Peak area analysis demonstrates ~10% and ~32% of NH_4NO_3 converts to N_2O on H-CHA-i and Cu/CHA-i, respectively. These results serve to demonstrate a few useful points: (1) even though NH_4NO_3 may only deposit at zeolite external surfaces during impregnation, it readily diffuses into zeolite pores and interacts

with BAS and/or Cu sites during TPD; (2) BAS clearly plays a catalytic role in NH_4NO_3 decomposition to N_2O, as proposed by prior studies;[54-56] (3) Cu-ions stabilize NH_4NO_3, leading to higher N_2O yield and desorption temperatures.

In **Figure 6b** on Cu/CHA-i impregnated with 0.6, 1.0, 2.0, 5.0 and 10.0 wt.% of NH_4NO_3, corresponding to NH_4NO_3/Cu-ion molar ratios of ~0.23, 0.38, 0.76, 1.99 and 4.21, respectively, measurements were carried out in 10% O_2/N_2 flow analogous to above. At NH_4NO_3 loadings $\leq$ 2.0 wt.%, N_2O formation follows a 2nd-order behavior, evidenced by (i) asymmetrical peak line shapes; (ii) decreased temperature of N_2O evolution with increased NH_4NO_3; and (iii) N_2O evolution peaks sharing a common trailing edge. Such characteristics suggest that (1) NH_4NO_3 is stabilized by NH_4NO_3 dissociation to NH_3 and HNO_3 (R13), followed by their separate adsorption on Cu or other zeolitic sites, and (2) N_2O formation is achieved by sequential reaction of NH_3 and HNO_3 on BAS. Possible N_2O formation pathways on BAS can be described by R14 and R15 as follows.[54-56]

$$NH_4NO_3 \rightleftharpoons NH_3 + HNO_3 \quad \text{R13}$$

$$HNO_3 + H^+ \rightarrow NO_2^+ + H_2O \quad \text{R14}$$

$$NH_3 + NO_2^+ \rightarrow N_2O + H_2O + H^+ \quad \text{R15}$$

At NH_4NO_3 loadings $\geq$ 5.0%, a new N_2O formation state is also developed that appears to follow a 1st-order behavior, characterized by an invariant temperature of ~265 °C. In this latter case, the 2nd-order N_2O formation state described above now appears as a shoulder peak. It is interesting to note that the 1st-order N_2O formation only appears when NH_4NO_3/Cu-ion molar ratio is above unity.

Based on **Figure 6a, 6b**, the energetically most favorable pathway for NH_4NO_3 decomposition to N_2O appears to be catalyzed by BAS (R13-R15); in the absence of Cu-ions, this chemistry leads to N_2O formation at ~215 °C. In the presence of Cu-ions, the chemisorption of NH_3 and HNO_3 on Cu delays their arrival at the BAS active sites, causing the N_2O formation temperature to rise. However, when the NH_4NO_3 content becomes higher than the combined molar contents of BAS and Cu-ions, for example 10 wt.%, a portion of NH_4NO_3 can only decompose to N_2O thermally

rather than catalytically. The ~265 °C N_2O formation state shown in **Figure 6a, 6b**, therefore, is readily attributed to thermal decomposition of NH_4NO_3. In addition to N_2O, NH_4NO_3 dissociation via R13 also leads to other catalytic reactions involving HNO_3 and NH_3, but without the formation of N_2O. Desorption profiles of NO, NO_2 and NH_3 are presented in **Figure S15a-c**. Formation pathways of these species will be briefly mentioned below but will not be a focus for the present study.

In **Figure 6c**, measurements were also conducted on 5 wt.% NH_4NO_3-loaded Cu/CHA-i in NH_3+O_2/N_2 and NO+NH_3+O_2/N_2 (i.e., standard SCR) flows, and the N_2O formation profiles for these measurements are compared to the analogous results under O_2/N_2 flow. Under NH_3+O_2/N_2 flow, total N_2O yield decreases to ~half that under O_2/N_2 flow, and the leading-edge temperature increases ~50 °C. Two explanations for these observations may apply: (1) NH_3 hinders NH_4NO_3 dissociation via R13; (2) NH_3 adsorbs on BAS to form NH_4^+, which hinders R14+R15. For TPD measured in NO+NH_3+O_2/N_2 (i.e., standard SCR flow), two local N_2O formation maxima are observed at ~240 and ~270 °C, respectively, and total N_2O yield becomes much lower than the other two measurements. Since the ~270 °C state is absent under typical standard SCR conditions (**Figure 4**), it is readily attributed to thermal decomposition of NH_4NO_3. The ~240 °C state, on the other hand, is likely a combination of standard SCR, NH_4NO_3 promoted SCR (R7),[14] and NH_4NO_3 decomposition catalyzed by BAS. Results shown in **Figure 6c** confirm again that in the presence of SCR reactants, the majority of NH_4NO_3 is consumed by R7 rather than by R5.[14]

3.5.2. TPD studies of "in situ" NH_4NO_3.

The H-zeolites and Cu catalysts used in Section 3.4 were applied here for TPD studies, aiming at understanding N_2O formation from the decomposition of NH_4NO_3 formed "in situ" during SCR. "In situ" NH_4NO_3 formation was achieved by running fast SCR at 100 °C as described in the Methods Section. At this low temperature, R4 rather than the target reaction R10 dominates, leading to the deposition of solid NH_4NO_3 on the catalyst. **Figure S16a-e** presents NH_3 and NOx desorption profiles over the 5 H-zeolites as a function of temperature. Since the desorption profiles are highly similar across all samples, the desorption of NO_2, NO and NH_3 is collectively described. The release of NO_2 centered at ~220 °C can be described by R16, where HNO_3 originates from NH_4NO_3 dissociation via R13. Upon NO_2 formation, the reverse of R11 also occurs to some extent,

leading to the generation of small amounts of NO at ~230 °C. The desorption profiles of NH_3 are more complex, displaying three features: one below 200 °C due to NH_3 adsorbed on weak acid sites (e.g., extra-framework Al), one between 200 and 300 °C due to NH_4NO_3 dissociation via R13, and one above 300 °C due to NH_3 adsorbed on BAS (i.e., NH_4^+).

$$4HNO_3 \rightarrow 4NO_2 + 2H_2O + O_2 \qquad \text{R16}$$

Figure 7a presents N_2O desorption profiles for the H-form samples compiled from **Figure S16,** noting that N_2O yields are all substantially higher than their respective NO_2 + NO yields. Over all samples except H-LTA, two N_2O formation peaks are observed at ~210-220 °C and ~260-270 °C. From the results in **Figure 6**, we can attribute the ~210-220 °C peak to BAS-catalyzed NH_4NO_3 decomposition and the ~260-270 °C peak to thermal decomposition of NH_4NO_3. Since LTA has a larger cage size than CHA and AEI, this may reduce confinement effects making NH_4NO_3 thermal decomposition more facile, rendering intimate overlapping of the two states to one N_2O formation peak at ~230 °C. **Figure 7b** presents H_2O desorption profiles of the H-form samples. H_2O signals mimic the corresponding N_2O signal line shapes, and display N_2O/H_2O intensity ratios of ~0.5, demonstrating that R5 occurs preferentially to R13+R16 during TPD on the H-form catalyst and consistent with much higher N_2O yields versus NO_2 and NO.

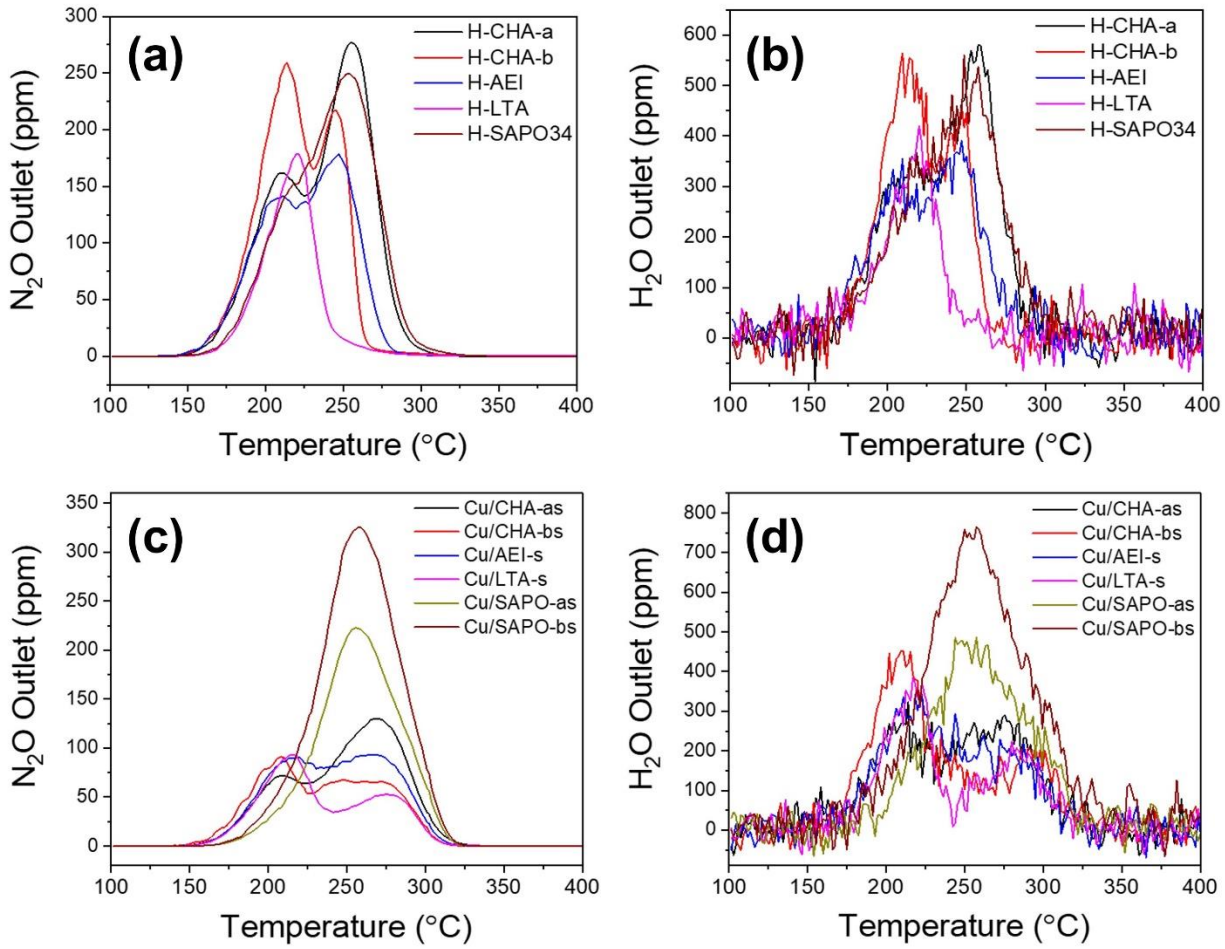

Figure 7. N_2O and H_2O outlet concentration as a function of temperature in temperature-programmed desorption (TPD) following "in situ" NH_4NO_3 deposition on H-form zeolites and the corresponding Cu-form catalysts. (a) N_2O, H-form; (b) H_2O, H-form; (c) N_2O, Cu-form; (d) H_2O, Cu-form. 120 mg catalyst, 10% O_2/N_2 gas flow 600 ml/min, ramping rate 3 °C/min.

The same TPD measurements were also carried out on the SSIE Cu catalysts. NH_3 and NOx desorption profiles as a function of temperature are depicted in **Figure S17a-f**. Compared with the H-form results in **Figure S16**, NO_2 yields on the Cu catalysts are markedly higher. This is likely due to accelerated HNO_3 decomposition (R16) that results from increased kinetic influence of NH_4NO_3 dissociation (R13) which is assisted by Cu-ions strongly binding the NH_3 formed from R13 (i.e., binding more strongly than HNO_3). Interestingly, NO_2 yields on the Cu/SAPO-34 samples are substantially lower than those on Cu/zeolites, further confirming our notion above that the SAPO-34 support plays a unique role stabilizing NH_4NO_3. This is also supported by the fact

that high-temperature NH_3 yields on the Cu/zeolites (i.e., NH_3 formed via $NH_4^+ \rightarrow NH_3 + H^+$) are substantially lower than their H-zeolite counterparts. This supports the notion of Cu-ions strongly binding NH_3 from R13 and suggests the presence of Cu-catalyzed NH_3 consumption reactions during TPD, e.g., described by R17. However, high-temperature NH_3 yields on H-SAPO-34 and the two Cu/SAPO-34 samples are rather similar. Such a difference corroborates the notion that NH_4NO_3 has higher stability on SAPO-34.

$$2NH_3 + 3NH_4NO_3 \rightarrow 4N_2 + 9H_2O \qquad \text{R17}$$

Figures 7c and **7d** plot N_2O and H_2O desorption profiles, respectively, for the Cu samples. Like their H-form counterparts, the 4 Cu-zeolite samples also show BAS catalyzed N_2O formation at ~210 °C. Interestingly, the two Cu/SAPO-34 samples do not display well-resolved peaks at low temperature, and N_2O yields are also substantially lower. At high temperature, in addition to the thermal N_2O formation state around 260 °C, all Cu samples display another weak state at ~280 °C that will be addressed in more detail below. N_2O/H_2O signal intensity ratios for the Cu catalysts are lower than 0.5, particularly below ~250 °C. As discussed earlier, unlike the H-form samples where R5 predominates, SCR reactions (e.g., R17) also occur on the Cu catalysts that are likely facilitated with greater kinetic influence of R13.

To clarify N_2O formation differences on H-form and Cu samples, selected N_2O desorption profiles in **Figures 7a** and **7c** are replotted for direct comparison and shown in **Figure 8**. N_2O yield on each Cu sample is lower than its corresponding H-form sample which we attribute, as noted above, to SCR reactions occurring on the Cu samples in addition to R5. N_2O release from the Cu-form samples also shifts to slightly higher temperature versus the H-form samples, which supports the notion of low temperature N_2O formation catalyzed by BAS and not Cu, and recognizing that Cu-exchange reduces BAS density. Lastly, over all the Cu catalysts, N_2O formation is extended to higher temperatures, e.g., for Cu/LTA, a well-resolved N_2O peak exists at ~280 °C that is absent on H-LTA. Since this temperature is higher than thermal decomposition temperature of NH_4NO_3 (~265 °C, **Figure 6**), it is unlikely associated with NH_4NO_3. Rather, the ~280 °C state can be attributed to R8, i.e., decomposition of an NH_4NO_3-like intermediate, Cu-NO_3[NH_3], that has been suggested to possess higher thermal stability than NH_4NO_3. [18, 19]

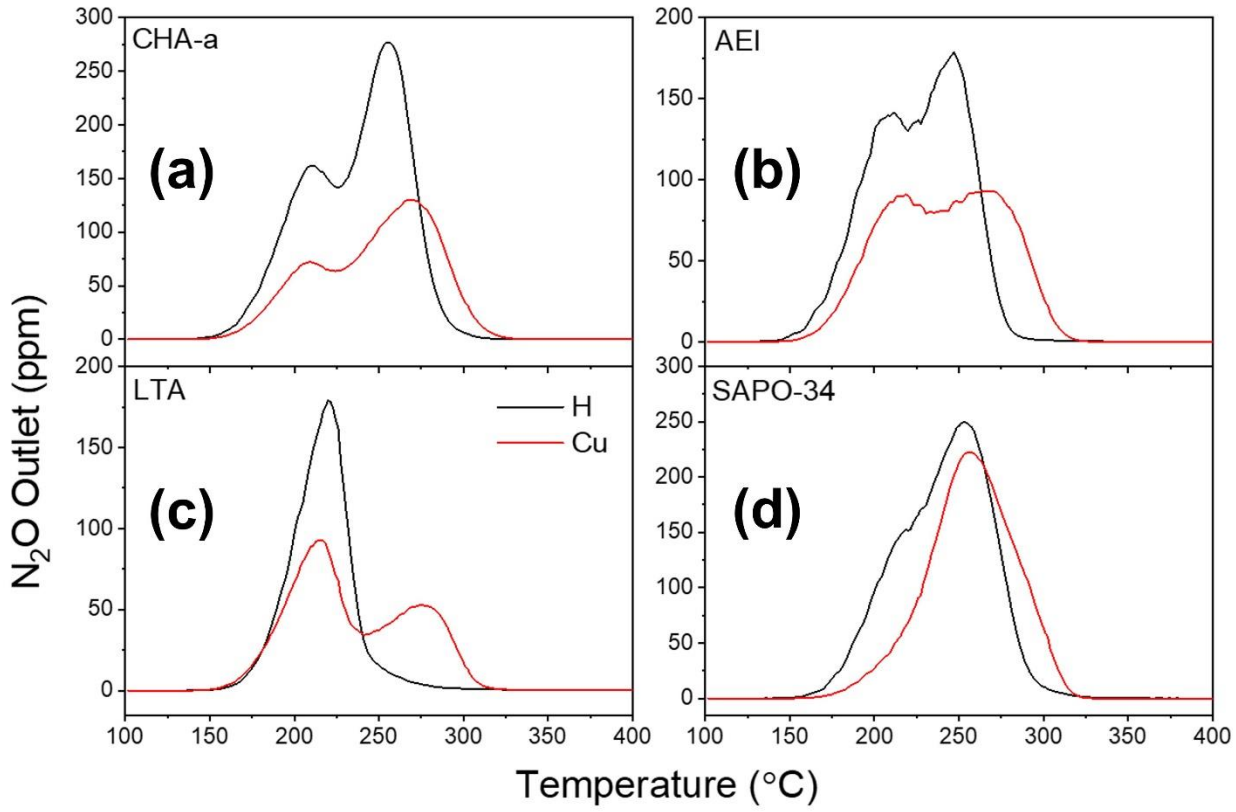

Figure 8. N_2O outlet profiles shown in **Figure 7** replotted for better direct comparison between H-form samples (black) and the corresponding Cu-form catalysts (red). (a) CHA-a; (b) AEI; (c) LTA; (d) SAPO-34.

3.6. Generalizing N_2O Formation Pathways.

We described in the Introduction section that the traditional wisdom regarding low-temperature N_2O formation during NH_3-SCR states that it is due to NH_4NO_3 decomposition, and gas phase NO_2 facilitates NH_4NO_3 formation (R4+R5). A few recent publications, however, proposed that low-temperature N_2O formation is irrelevant to NH_4NO_3. For example, Xi et al.,[22] based on the absence of nitrate bands from in situ DRIFTS experiments and the argument about inconsistencies between high stability of NH_4NO_3 and N_2O formation at low temperatures, excluded the formation of surface nitrate or NH_4NO_3 as a precursor of N_2O. We note here that in situ DRIFTS studies may not lead to unambiguous conclusions regarding the presence/absence of surface nitrates. Under the DRIFTS experimental conditions Xi et al. used, i.e., ~20 mg Cu/CHA catalyst under a reactant flow with space velocity of ~60k h^{-1}, the amount of NH_4NO_3 needed to sustain ~10 ppm of N_2O

formation (assuming N_2O originates entirely from NH_4NO_3 decomposition) only comprises ~0.1% of the catalyst mass. Such an NH_4NO_3 concentration is at best at the borderline of detection via FTIR. Moreover, the argument that NH_4NO_3 is too stable to decompose to N_2O at low temperatures,[22] also needs reconsideration. Although thermal decomposition of NH_4NO_3 occurs well above 200 °C, catalytic decomposition by BAS occurs at much lower temperatures. Our TPD measurements on both impregnated (**Figure 6**) and reactively formed (**Figure 7**) NH_4NO_3 reveal N_2O formation as low as ~150 °C. Note that the onset of N_2O formation during steady-state SCR occurs at similar temperatures (**Figure 4**). Furthermore, the statement by Shih et al.[6] that $E_{a,\ N2O}$ and $E_{a,\ SCR}$ values over the same catalyst are indistinguishable, and based on which the authors proposed that N_2O forms during the reduction half-cycle involving NH_3-solvated Cu-NH_3NO intermediates aided by oxygen donors (zeolite lattice O, H_2O, or O_2), also appears problematic. Our results shown in **Figure 2** demonstrate clearly that $E_{a,\ N2O}$ and $E_{a,\ SCR}$ values over many catalysts studied here are rather different.

The $E_{a,\ SCR}$ and $E_{a,\ N2O}$ comparison results shown in **Figure 2** are further discussed here to elucidate whether proposals claiming that low temperature N_2O originates from highly unstable intermediates, for example NH_2NO or NH_3NO, can be justified. We note first that, since N_2O formation rates are always much lower than SCR rates (**Figure 3**), it is highly unlikely that the same unstable intermediates (e.g., NH_2NO) are involved in both N_2 and N_2O formation when $E_{a,\ N2O} < E_{a,\ SCR}$. This follows since, from simple kinetic arguments, lower activation barrier pathways should lead to products with higher yields. Furthermore, steady-state kinetics data comparison between Cu/SSZ-13 and Cu/SAPO-34 reveals strong evidence against the proposal that low temperature N_2O originates from highly unstable intermediates. Note that these two catalysts are isostructural and the nature of SCR active Cu species are identical;[57, 58] note also that at similar $E_{a,\ SCR}$, Cu/SAPO-34 samples display substantially lower $E_{a,\ N2O}$ than Cu/SSZ-13 (**Figure 2**). As such, much higher N_2O formation rates on Cu/SAPO-34 are anticipated from simple kinetic arguments, contradicting the experimental results (**Figure 3**).

Based on our steady-state SCR and TPD data, $E_{a,\ N2O}$ values are influenced by multiple factors including (1) Cu loading and speciation: higher Cu loading, and particularly higher ZCuOH population, lead to increase in $E_{a,\ N2O}$ (**Figure 1c**); (2) zeolite support Si/Al ratio: higher Si/Al ratio leads to increase in $E_{a,\ N2O}$ (**Figure S2e**); (3) catalyst contamination: sulfur poisoning leads to

increase in $E_{a,\ N2O}$ (**Figure S4e**); (4) nature of the support: zeolite supports leads to higher $E_{a,\ N2O}$ than SAPO-34 (**Figure S8e**). These experimental observations can only be rationalized invoking the participation of NH_4NO_3 in low temperature N_2O formation, where three key factors influence $E_{a,\ N2O}$ values and $\frac{r_{N_2O}}{r_{SCR}}$ ratios, including (1) in situ NH_4NO_3 formation pathways and how facile they are; (2) the level of participation of BAS; and (3) the competition between R5 and R7. More discussions are given immediately below.

Our TPD data shown in **Figure 6** through **Figure 8** demonstrate the presence of three N_2O formation pathways: BAS catalyzed NH_4NO_3 decomposition (~215 °C), thermal decomposition of NH_4NO_3 (~265 °C), and thermal decomposition of NH_4NO_3-like species (~280 °C). As such, steady-state $E_{a,\ N2O}$ contains contributions from all three pathways with varying weights depending on the nature of the catalyst. This explains why Cu/CHA samples with high Si/Al ratios display substantially higher $E_{a,\ N2O}$ values than their low Si/Al counterparts (**Figure 2**): the lack of BAS participation leads to high $E_{a,\ N2O}$, and vice versa.

Regarding the competition between R5 and R7, two salient points are worth noting. First, NH_4NO_3 stabilization under steady-state operations leads to reduced N_2O formation, as clearly demonstrated by prior comparative studies between small-pore and medium/large pore Cu-zeolite catalysts.[5, 13] In the present study, we show that SAPO-34 support provides additional NH_4NO_3 stabilization leading to even lower steady-state N_2O formation and, accordingly, low steady-state $E_{a,\ N2O}$ values (**Figure 3**). On the other hand, rapid variations of catalyst temperature, as in the case of TPD (or transient SCR operations under practical on-road conditions), lead to N_2O release "spikes" over catalysts that stabilize NH_4NO_3 (**Figure 7c**). This latter notion has also been reported by Olsson and coworkers.[13]

Regarding in situ NH_4NO_3 formation, we limit our discussions only to standard SCR conditions (i.e., in the absence of gaseous NO_2 supply). In this case, two scenarios can be considered: (1) in situ NO oxidation to NO_2 followed by NH_4NO_3 formation via R4, and (2) NH_4NO_3 formation without the presence of in situ NO_2. Regarding NO oxidation to NO_2, we show in **Figure S10** that CuO readily oxidizes NO to NO_2 to enable fast SCR (R10), and N_2O formation proceeds via R4+R5. For catalysts with negligible CuO, prior studies have demonstrated that (i) N_2O forms during the reduction half cycle of SCR (i.e., in the absence of O_2),[6] and (ii) clear positive

correlations exist between $ZCu^{II}OH$ and N_2O formation.[16, 17] This latter note is also supported by our data here (**Figure S9**). As such, we propose here the following pathways for in situ NO_2 formation.

$$ZCu^{II}OH + NO \rightarrow ZCu^{I} + HONO \quad \text{R18}$$

$$ZCu^{II}OH + HONO \rightarrow ZCu^{I} + NO_2 + H_2O \quad \text{R19}$$

We note that, via a chemical trapping method, R18 has been demonstrated to occur on Cu-ions in the absence of NH_3.[59] On NH_3-solvated Cu-ions, the feasibility of this reaction has also been demonstrated computationally.[51] Below, we use DFT calculations to further probe R18+R19.

It has been clearly documented in recent literature that the oxidation half cycle of standard NH_3-SCR is achieved by the interaction between O_2 and a pair of $[Cu^{I}(NH_3)_2]^+$ to form di-Cu complexes via R20.[51, 60, 61]

$$2[Cu^{I}(NH_3)_2]^+ + O_2 \rightarrow [Cu^{II}{}_2(NH_3)_4O_2]^{2+} \quad \text{R20}$$

The reactivity of $[Cu^{II}{}_2(NH_3)_4O_2]^{2+}$ complexes toward NO, NH_3, or NO+NH_3 has been studied by Negri et al.[60] However, they did not report N_2O formation during such reactions. Importantly, di-Cu complexes must split back to monomeric Cu species for continuous catalytic turnovers. This is because if these complexes were to form and remain intact without splitting, then it would not account for the significant impact of Cu loading on SCR kinetics nor the prevalence of monomeric Cu species observed through operando spectroscopies.[23, 62, 63] Since $[Cu^{II}{}_2(NH_3)_4O_2]^{2+}$ complexes maintain high reactivity towards NO, we postulate the follow reaction pathways for NO_2 formation, followed by di-Cu splitting via hydrolysis.

$$[Cu^{II}{}_2(NH_3)_4O_2]^{2+} + NO \rightarrow [Cu^{II}{}_2(NH_3)_4O]^{2+} + NO_2 \quad \text{R21}$$

$$[Cu^{II}{}_2(NH_3)_4O]^{2+} + 2NH_3 + H_2O \rightarrow 2[Cu^{II}(NH_3)_3OH]^+ \quad \text{R22}$$

In the following, DFT calculations will also be applied to probe energetics of possible reaction pathways for R21.

Possible NH_4NO_3 formation pathways without the participation of NO_2 are also addressed here. In this case, two scenarios can be considered: (1) direct NO activation to Cu-bound nitrate followed by its interaction with NH_3 to form NH_4NO_3, and (2) oxidation of SCR intermediates, e.g., NH_4NO_2, to NH_4NO_3. Regarding the first scenario, literature has repeatedly reported the facile formation of ZCu^{II}-NO_3^- via interaction between ZCu^I and $NO+O_2$. Above low-temperature SCR light-off temperatures, the formation of such nitrates only becomes spectroscopically evident in the absence of NH_3.[64-66] Moreover, Negri et al. demonstrated that at 50 °C, mixed-ligand $[Cu^{II}(NH_3)_3(NO_3)]^+$ complexes become stable enough to be spectroscopically detected.[65] Furthermore, our TPD results in **Figure 8** clearly demonstrate the presence of a ~280 °C N_2O formation state that is most consistent with decomposition of mixed-ligand Cu-$NO_3[NH_3]$. As such, it is conceivable that under low-temperature SCR conditions, $[Cu^I(NH_3)_2]^+$ complexes may interact with $NO+O_2$ to form transient mixed-ligand complexes, and the latter can then decompose to release N_2O via R8 or hydrolyze to NH_4NO_3 via R9. Regarding NH_4NO_2 oxidation to NH_4NO_3 as suggested recently by Yao et al.,[17] since NH_4NO_2 is considered highly unstable by many, it is difficult to ascertain if this species has sufficient residence time to be oxidized, not to mention detailed oxidation pathways. As in the case of R13 for NH_4NO_3, NH_4NO_2 likely also establishes solid-gas equilibrium via $NH_4NO_2 \rightleftharpoons NH_3 + HONO$ under low-temperature SCR conditions to extend its residence time. In this sense, R19, followed by non-selective reactions involving NO_2, may better describe N_2O formation.

3.7. DFT Calculations.

To preface this section, it is important to reiterate that, under low-temperature standard SCR conditions, the process of {in situ NO_2 formation} → {NH_4NO_3 formation} → {catalytic decomposition to N_2O} aligns more closely with prior experimental observations and is supported by the data presented above. However, the remarkable complexity of N_2O formation (e.g., as evident from our steady-state and TPD data) suggests the coexistence of multiple N_2O formation pathways. Therefore, our focus here is on three types of calculations:

1. NO oxidation to NO_2 on monomeric and dimeric Cu-ions, with the understanding that CuO clusters also play a role in catalyzing this reaction. However, reaction paths on CuO will not be calculated here. Also note that upon NO_2 formation, N_2O readily forms via R4+R5.

Since these subsequent reaction pathways have been extensively studied in the past, these are not a focus of our calculations here.

2. O_2 adsorption on $[Cu^I(NH_3)_2]^+$ to form NH_3-Cu-O_2 complexes, followed by NH_3 activation by the adsorbed oxygen to form intermediates that further convert to N_2O. Note that this particular calculation aims to elucidate how N_2O forms under NH_3 oxidation conditions.

3. NO+O_2 adsorption on $[Cu^I(NH_3)_2]^+$ to form NH_3-Cu-NO_3 complexes, followed by its decomposition to release N_2O. Note that $[Cu^I(NH_3)_2]^+$ is the most stable Cu^I intermediate under low-temperature SCR, and the chemisorption of both O_2 and NO+O_2 are thermodynamically feasible on isolated Cu^I.[67]

To facilitate our mechanistic calculations, we first calculated Cu and O Bader charges of a few complexes that are likely or demonstrated intermediates for low-temperature SCR and form when O_2 interacts with ZCu^I and $Z[Cu^I(NH_3)_2]$, including ZCu-O_2, ZCu-O-O, Cu$(NH_3)_2$-O_2-Cu$(NH_3)_2$, Cu$(NH_3)_2$-O-O-Cu$(NH_3)_2$ and Cu$(NH_3)_2$-O-Cu$(NH_3)_2$. It is important to note that O_2 can interact with Cu centers via both "side-on" and "end-on" configurations, which we have denoted as "-O_2" and "-O-O", respectively. Our analysis, as depicted in **Figure S18**, indicates that the formation of these complexes typically leads to Cu oxidation from +1 to +2 oxidation state with the accompanying O remaining as O_2^-, O_2^{2-}, or O^{2-} to maintain charge balance. Furthermore, it is observed that the "side-on" configuration facilitates greater charge transfer from Cu to O compared to the "end-on" configuration. Notably, another important intermediate, ZCu-NO_3, that forms when ZCu^I interacts with NO+O_2, is not calculated here as previous electronic paramagnetic resonance (EPR) studies have unequivocally demonstrated that this reaction leads to Cu oxidation from +1 to +2 oxidation state.[64, 68, 69]

The stepwise NO oxidation process was calculated on ZCu$(NH_3)_3$OH, first to HONO and then to NO_2 (R18+R19). Note that each oxidation step involves the transfer of one electron from Cu to NOx, requiring two ZCu$(NH_3)_3$OH to enable NO_2 formation. The results shown in **Figure 9a** reveal three distinct steps in each oxidation pathway: (i) NO (or HONO) approaches the Cu-OH site → (ii) the Cu-HONO (or Cu-OH[HONO]) complex forms → (iii) the complex decomposes to release HONO (or NO_2). The calculated Gibbs free energies along the reaction coordinates indicates that NO oxidation to HONO is slightly endergonic while HONO oxidation to NO_2 is

moderately exergonic. Importantly, the activation barriers for the formation of the transition states are exceedingly low and demonstrate the feasibility of these reaction pathways. Furthermore, the more challenging HONO oxidation step aligns with the low N_2O selectivity observed during standard SCR. This is consistent with N_2 formation during standard SCR being sustained upon NO activation to HONO, whereas only N_2O formation requires further oxidation of HONO to NO_2.

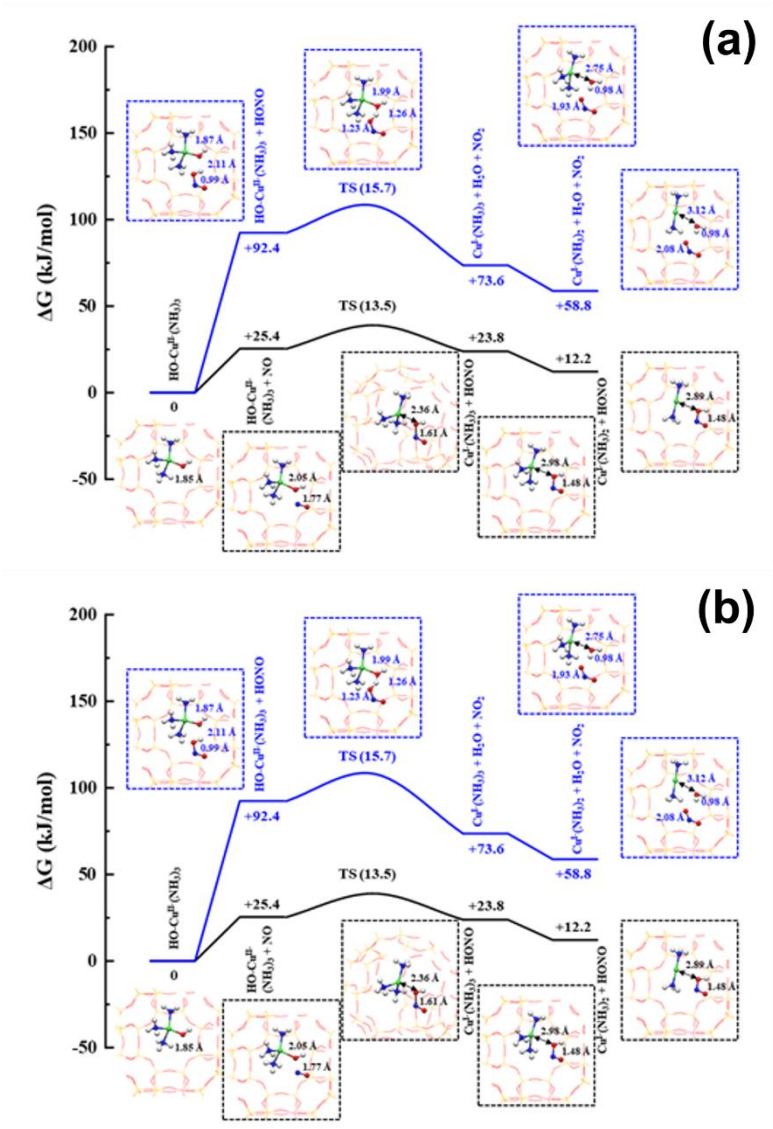

Figure 9. DFT-calculated energy landscapes and key bond lengths & distances for the oxidation of NO to NO_2 by (a) NH_3-solvated monomeric Cu-OH site via sequential oxidation, and (b) NH_3-solvated dimeric Cu-O-O-Cu or Cu-O_2-Cu sites. Color code: green, Cu; blue, N; red: O; white: H.

The oxidation of NO by the peroxo diamino dicopper complexes $Cu(NH_3)_2$-O_2-$Cu(NH_3)_2$ and $Cu(NH_3)_2$-O-O-$Cu(NH_3)_2$ was calculated, and the results are illustrated in **Figure 9b**. It is observed that the placement of NO adjacent to these complexes necessitates higher energies compared to placing NO next to $ZCu(NH_3)_3OH$, as depicted in **Figure 9a**. Furthermore, the placement of NO next to the more rigid $Cu(NH_3)_2$-O_2-$Cu(NH_3)_2$ requires higher energy than placing NO next to the more flexible $Cu(NH_3)_2$-O-O-$Cu(NH_3)_2$. These results can be rationalized by considering entropy losses, i.e., complexing NO with bulkier and more rigid moieties entails a higher entropy penalty. Nevertheless, the activation barriers for the formation of the Cu_2-NO complexes remain relatively low, indicating the feasibility of R21.

The possible N_2O formation pathways from NH_3-Cu-O_2 or NH_3-Cu-NO_3 intermediates were calculated, and the detailed Gibbs free energies along the reaction coordinates are shown in **Figure S19** and **Figure S20**, respectively. The key findings indicate that NH_3 activation by oxygen adsorbed on Cu involves N-H bond cleavage and O transfer steps, leading to the formation of a Cu-ONH complex. Subsequently, the coupling of two such complexes facilitates N_2O formation with two activation barriers over 100 kJ/mol found along the reaction coordinates. As for NH_3-Cu-NO_3 intermediates, the Cu-bound nitrate reacts with NH_3 to form Cu-bound NH_4NO_3-like species which further decomposes to release N_2O; three activation barriers over 100 kJ/mol found along these reaction coordinates. These results suggest the unlikelihood of these mechanisms serving as possible pathways for low-temperature N_2O formation during SCR.

Our comprehensive calculations provide substantial evidence to support our experimental findings. We have confirmed that the presence of NO_2 in the reactant feed results in NH_4NO_3 formation and its subsequent catalytic decomposition on BAS, which is a widely accepted mechanism for low-temperature N_2O formation during SCR. Even in the absence of NO_2 in the feed, in situ NO_2 formed from CuO-catalyzed NO oxidation facilitates N_2O formation via the same mechanism. Furthermore, our DFT calculations depicted in **Figure 9** illustrate that ZCuOH and $Z_2Cu_2O_2$ sites also catalyze NO oxidation to NO_2 with surmountable energy barriers. Therefore, low-temperature N_2O formation under both standard and fast NH_3-SCR conditions can be generally described by R4+R5. Lastly, we have demonstrated that direct N_2O formation pathways on Cu-ions, such as NH_3 interacting with either adsorbed oxygen species or with nitrate, require relatively high activation energies, thus making them unlikely contributors to low-temperature

N_2O formation. This aligns with our comparative studies between H- and Cu-zeolites (**Figure 6** & **Figure 8**), where Cu delays rather than facilitates low-temperature N_2O formation. As a result, we cannot substantiate the claims that low-temperature N_2O formation is linked to a low-barrier NO + NH_3 reaction over Cu-sites,[21] as this would imply that Cu-ions both promote and hinder low-temperature N_2O formation simultaneously.

3.8. Low-Temperature N_2O Formation Network.

Herein we provide a (maybe incomplete) N_2O formation network during low-temperature NH_3-SCR over Cu-exchanged zeolite catalysts, shown in **Figure 10**. This schematic model includes (1) "NO_2 pool" contributed by NO oxidation catalyzed by both CuO and isolated Cu-ions, and gaseous NO_2 supply; (2) NH_4NO_3 formation from NO_2 and NH_3, as well as interconversions between NH_4NO_3 and Cu-bound NH_4NO_3-like moieties; (3) NH_4NO_3 consumption by SCR reactions; and (4) N_2O formation from decomposition of NH_4NO_3 and NH_4NO_3-like species, either catalytically or thermally. It is our belief that this model is consistent with most experimental observations shown here and reported by others. We are in the process of generating a generally applicable mathematic model on N_2O formation which will be reported elsewhere.

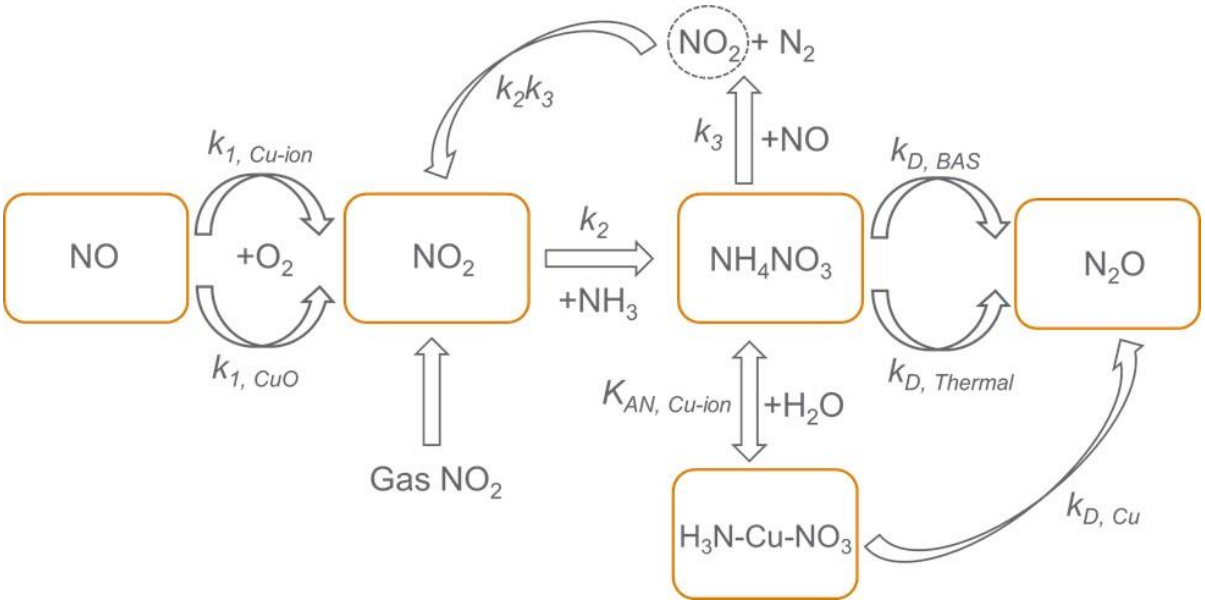

Figure 10. Schematic of N_2O formation pathways during low temperature NH_3-SCR over Cu SCR catalysts.

4. CONCLUSIONS

To elucidate formation mechanisms of side product N_2O in low-temperature standard NH_3-SCR over small pore Cu-exchanged zeolites, more than 50 catalyst samples are used here to ensure "completeness" of catalytic properties and "representativeness" of our data collection. This strategy enables unprecedented comprehensive comparisons between steady-state reaction $E_{a,\ SCR}$ and $E_{a,\ N2O}$, leading to the conclusions that (1) low-temperature N_2O formation must involve NH_4NO_3, and (2) low-temperature N_2O formation occurs via more than one reaction pathways. By measuring low temperature $\frac{r_{N_2O}}{r_{SCR}}$ ratios, we can further conclude that Cu moieties that facilitate in situ NO oxidation to NO_2, i.e., $ZCu^{II}OH$ and CuO, also facilitate N_2O formation. This leads to an important conclusion that in the absence of gaseous NO_2 in the reactant, NH_4NO_3 originates from interaction between NH_3 and in situ NO_2. Through detailed TPD studies on H-zeolite supports and Cu catalysts, three N_2O formation channels are identified, including BAS catalyzed NH_4NO_3 decomposition, thermal NH_4NO_3 decomposition, and decomposition of Cu-bound NH_4NO_3-like species, respectively, occurring in the order of increasing temperature. DFT calculations corroborate our experiment-oriented conclusions by demonstrating that $ZCu^{II}OH$ catalyzes NO oxidation to NO_2 via low energy barrier pathways, and direct N_2O formation from Cu-bound intermediates typically involve much higher energy barriers. Finally, a comprehensive N_2O formation network is provided.

DECLARATION OF COMPETING INTEREST

The authors declare that they have no known competing financial interests or personal relationships that could have appeared to influence the work reported in this paper.

SUPPLEMENTARY MATERIAL: Names, compositions, sources, and synthesis methods of the zeolites, Cu-catalysts, and SAPO-34, additional details of the catalyst synthesis and treatment methods, additional NOx conversion and N_2O selectivity data including Arrhenius plots, activation energy comparisons, and N_2O and SCR reaction rate comparisons, time-on-stream data, and additional TPD results.

ACKNOWLEDGMENT

The authors gratefully acknowledge the U.S. Department of Energy (DOE), Energy Efficiency and Renewable Energy (EERE), Vehicle Technologies Office for the financial support of this work. The research described in this paper was in-part performed at the Environmental Molecular Sciences Laboratory (EMSL), a national scientific user facility sponsored by the DOE's Office of Biological and Environmental Research and located at PNNL. PNNL is operated for the DOE by Battelle under contract number DE-AC05-76RL01830. The authors greatly appreciate Dr. Jim Hughes from Zeolyst Inc. for kindly providing proprietary Cu/SAPO-34 samples. FG is also very thankful to Profs. Enrico Tronconi and Isabella Nova (Politecnico di Milano) and Prof. Chris Paolucci (University of Virginia) for fruitful discussions.

CREDIT AUTHOR STATEMENT

Yilin Wang: Investigation, Writing – original draft, Project administration; **Wenru Zhao**: Software; **Yiqing Wu**: Investigation; **Eric D. Walter**: Investigation, Formal analysis; **Kenneth G. Rappé**: Writing – original draft, Writing – review & editing, Supervision, Project administration, Funding acquisition; **Yong Wang**: Writing – review & editing, Supervision, Funding acquisition; **Suk Bong Hong**: Resources; **Donghai Mei**: Methodology, Software, Writing – original draft, Writing – review & editing; **Feng Gao**: Conceptualization, Methodology, Investigation, Formal analysis, Resources, Writing – original draft, Writing – review & editing, Supervision.

REFERENCES

1. A. M. Beale; F. Gao; I. Lezcano-Gonzalez; C. H. F. Peden, J. Szanyi. Recent advances in automotive catalysis for NOx emission control by small-pore microporous materials. *Chemical Society Reviews* **2015**, *44* (20), 7371-7405, 10.1039/C5CS00108K. DOI: 10.1039/C5CS00108K.
2. L. P. Han; S. X. Cai; M. Gao; J. Hasegawa; P. L. Wang; J. P. Zhang; L. Y. Shi; D. S. Zhang. Selective Catalytic Reduction of NOx with NH3 by Using Novel Catalysts: State of the Art and Future Prospects. *Chem Rev* **2019**, *119* (19), 10916-10976. DOI: 10.1021/acs.chemrev.9b00202.
3. E. Borfecchia; P. Beato; S. Svelle; U. Olsbye; C. Lamberti; S. Bordiga. Cu-CHA - a model system for applied selective redox catalysis. *Chemical Society Reviews* **2018**, *47* (22), 8097-8133. DOI: 10.1039/c8cs00373d.
4. R. Ravishankara; J. S. Daniel; R. W. Portmann. Nitrous Oxide (N2O): The Dominant Ozone-Depleting Substance Emitted in the 21st Century. *Science* **2009**, *326*, 123-125. DOI: 10.1126/science.1176985.
5. H. Y. Chen; Z. H. Wei; M. Kollar; F. Gao; Y. L. Wang; J. Szanyi; C. G. F. Peden. A comparative study of N2O formation during the selective catalytic reduction of NOx with NH3 on zeolite supported Cu catalysts. *J Catal* **2015**, *329*, 490-498. DOI: 10.1016/j.jcat.2015.06.016.

6. A. J. Shih; J. M. Gonzalez; I. Khurana; L. P. Ramirez; L. A. Pena; A. Kumar; A. L. Villa. Influence of ZCuOH, Z(2)Cu, and Extraframework CuxOy Species in Cu-SSZ-13 on N2O Formation during the Selective Catalytic Reduction of NOx with NH3. *Acs Catal* **2021**, *11* (16), 10362-10376. DOI: 10.1021/acscatal.1c01871.
7. M. P. Ruggeri; J. Y. Luo; I. Nova; E. Tronconi; K. Kamasamudram; A. Yezerets. Novel method of ammonium nitrate quantification in SCR catalysts. *Catal Today* **2018**, *307*, 48-54. DOI: 10.1016/j.cattod.2017.04.016.
8. G. Centi; S. Perathoner. Nature of Active Species in Copper-Based Catalysts and Their Chemistry of Transformation of Nitrogen-Oxides. *Appl Catal a-Gen* **1995**, *132* (2), 179-259.
9. S. Brandenberger; O. Krocher; A. Tissler; R. Althoff. The State of the Art in Selective Catalytic Reduction of NOx by Ammonia Using Metal-Exchanged Zeolite Catalysts. *Catal Rev* **2008**, *50* (4), 492-531. DOI: 10.1080/01614940802480122.
10. A. A. Verma; S. A. Bates; R. Anggara; C. Paolucci; A. A. Parekh; K. Kamasamudram; A. Yezerets; J. T. Miller; W. N. Delgass; W. F. Schneider; et al. NO oxidation: A probe reaction on Cu-SSZ-13. *J Catal* **2014**, *312*, 179-190. DOI: DOI 10.1016/j.jcat.2014.01.017.
11. H. Y. Chen; Z. H. Wei; M. Kollar; F. Gao; Y. L. Wang; J. Szanyi; C. H. F. Peden. NO oxidation on zeolite supported Cu catalysts: Formation andreactivity of surface nitrates. *Catal Today* **2016**, *267*, 17-27.
12. Y. L. Wang; R. Z. Zhao; K. G. Rappé; Y. Wang; F. L. Che; F. Gao. Mechanisms and Site Requirements for NO and NH3 oxidation on Cu/SSZ-13. *Applied Catalysis B: Environment and Energy* **2024**, *346*, 123726. DOI: 10.1016/j.apcatb.2024.123726.
13. J. Han; A. Y. Wang; G. Isapour; H. Harelind; M. Skoglundh; D. Creaser; L. Olsson. N2O Formation during NH3-SCR over Different Zeolite Frameworks: Effect of Framework Structure, Copper Species, and Water. *Ind Eng Chem Res* **2021**, *60* (49), 17826-17839. DOI: 10.1021/acs.iecr.1c02732.
14. P. Forzatti; I. Nova; E. Tronconi. Enhanced NH3 Selective Catalytic Reduction for NOx Abatement. *Angew Chem Int Edit* **2009**, *48* (44), 8366-8368. DOI: DOI 10.1002/anie.200903857.
15. D. Zhang; R. T. Yang. N2O Formation Pathways over Zeolite-Supported Cu and Fe Catalysts in NH3-SCR. *Energ Fuel* **2018**, *32* (2), 2170-2182. DOI: 10.1021/acs.energyfuels.7b03405.
16. B. Liu; D. W. Yao; F. Wu; L. Wei; X. W. Li; X. L. Wang. Experimental Investigation on N2O Formation during the Selective Catalytic Reduction of NOx with NH3 over Cu-SSZ-13. *Ind Eng Chem Res* **2019**, *58* (45), 20516-20527. DOI: 10.1021/acs.iecr.9b03294.
17. D. W. Yao; B. A. Liu; F. Wu; Y. X. Li; X. H. Hu; W. Y. Jin; X. L. Wang. N2O Formation Mechanism During Low-Temperature NH3-SCR over Cu-SSZ-13 Catalysts with Different Cu Loadings. *Ind Eng Chem Res* **2021**, *60* (28), 10083-10093. DOI: 10.1021/acs.iecr.1c01514.
18. M. Colombo; I. Nova; E. Tronconi. Detailed kinetic modeling of the NH3-NO/NO2 SCR reactions over a commercial Cu-zeolite catalyst for Diesel exhausts after treatment. *Catal Today* **2012**, *197* (1), 243-255. DOI: DOI 10.1016/j.cattod.2012.09.002.
19. M. Bendrich; A. Scheuer; R. E. Hayes; M. Votsmeier. Unified mechanistic model for Standard SCR, Fast SCR, and NO2 SCR over a copper chabazite catalyst. *Appl Catal B-Environ* **2018**, *222*, 76-87. DOI: 10.1016/j.apcatb.2017.09.069.
20. L. Negahdar; N. E. Omori, M. G. Quesne; M. D. Frogley; F. Cacho-Nerin; W. Jones; S. W. T. Price; C. R. A. Catlow; A. M. Beale. Elucidating the Significance of Copper and Nitrate Speciation in Cu-SSZ-13 for N2O Formation during NH3-SCR. *Acs Catal* **2021**, *11* (21), 13091-13101. DOI: 10.1021/acscatal.1c03174.
21. Y. X. Feng; T. V. W. Janssens; P. N. R. Vennestrom; J. Jansson; M. Skoglundh; H. Gronbeck. The Role of H+- and Cu+-Sites for N2O Formation during NH3-SCR over Cu-CHA. *J Phys Chem C* **2021**, *125* (8), 4595-4601. DOI: 10.1021/acs.jpcc.0c11008.

22. Y. Z. Xi; N. A. Ottinger; C. J. Keturakis; Z. G. Liu. Dynamics of low temperature N2O formation under SCR reaction conditions over a Cu-SSZ-13 catalyst. *Appl Catal B-Environ* **2021**, *294*. DOI: 10.1016/j.apcatb.2021.120245.
23. Y. Q. Wu; Y. Ma; Y. L. Wang; K. G. Rappé; N. M. Washton; Y. Wang; E. D. Walter; F. Gao. Rate Controlling in Low-Temperature Standard NH3-SCR: Implications from Operando EPR Spectroscopy and Reaction Kinetics. *J Am Chem Soc* **2022**, *144* (22), 9734-9746. DOI: 10.1021/jacs.2c01933.
24. Y. Q. Wu; T. Andana; Y. L. Wang; Y. Chen; E. D. Walter; M. H. Engelhard; K. G. Rappé; Y. Wang; F. Gao; U. Menon; et al. A comparative study between real-world and laboratory accelerated aging of Cu/SSZ-13 SCR catalysts. *Appl Catal B-Environ* **2022**, *318*. DOI: 10.1016/j.apcatb.2022.121807.
25. Y. Q. Wu; W. R. Zhao; S. H. Ahn; Y. L. Wang; E. D. Walter; Y. Chen; M. A. Derewinski; N. M. Washton; K. G. Rappe; Y. Wang; et al. Interplay between copper redox and transfer and support acidity and topology in low temperature NH3-SCR. *Nat Commun* **2023**, *14* (1). DOI: 10.1038/s41467-023-38309-8.
26. F. Gao; E. D. Walter; E. M. Karp; J. Y. Luo; R. G. Tonkyn; J. H. Kwak; J. Szanyi; C. G. F. Peden. Structure-activity relationships in NH3-SCR over Cu-SSZ-13 as probed by reaction kinetics and EPR studies. *J Catal* **2013**, *300*, 20-29. DOI: DOI 10.1016/j.jcat.2012.12.020.
27. F. Gao; E. D. Walter; M. Kollar; Y. L. Wang; J. Szanyi; C. H. F. Peden. Understanding ammonia selective catalytic reduction kinetics over Cu/SSZ-13 from motion of the Cu ions. *J Catal* **2014**, *319*, 1-14. DOI: DOI 10.1016/j.jcat.2014.08.010.
28. R. Q. Long; R. T. Yang. Selective catalytic reduction of NO with ammonia over Fe(3+)-exchanged mordenite (Fe-MOR): Catalytic performance, characterization, and mechanistic study. *J Catal* **2002**, *207* (2), 274-285. DOI: DOI 10.1006/jcat.2002.3521.
29. Y. Cui; F. Gao. Cu Loading Dependence of Fast NH3-SCR on Cu/SSZ-13. *Emission Control Science and Technology* **2019**, *5* (2), 124-132. DOI: https://doi.org/10.1007/s40825-019-00117-2.
30. J. VandeVondele; M. Krack; F. Mohamed; M. Parrinello; T. Chassaing; J. Hutter. QUICKSTEP: Fast and Accurate Density Functional Calculations Using a Mixed Gaussian and Plane Waves Approach. *Comput. Phys. Commun.* **2005**, *167*, 103-128. DOI: 10.1016/j.cpc.2004.12.014.
31. J. Hutter; M. Iannuzzi; F. Schiffmann; J. VandeVondele. CP2K: Atomistic Simulations of Condensed Matter Systems. *Wiley Interdiscip. Rev.: Comput. Mol. Sci.* **2014**, *4* (1), 15-25. DOI: 10.1002/wcms.1159.
32. J. P. Perdew; K. Burke; Y. Wang. Generalized Gradient Approximation for the Exchange-Correlation Hole of a Many-Electron System. *Phys. Rev. B* **1998**, *57* (23), 14999-14999. DOI: 10.1103/PhysRevB.57.14999.
33. A. Govind Rajan; M. S. Strano; D. Blankschtein. Ab Initio Molecular Dynamics and Lattice Dynamics-Based Force Field for Modeling Hexagonal Boron Nitride in Mechanical and Interfacial Applications. *J. Phys. Chem. Lett.* **2018**, *9* (7), 1584-1591. DOI: 10.1021/acs.jpclett.7b03443.
34. J. VandeVondele; J. Hutter. Gaussian Basis Sets for Accurate Calculations on Molecular Systems in Gas and Condensed Phases. *J. Chem. Phys.* **2007**, *127*, 114105. DOI: 10.1063/1.2770708.
35. S. Grimme; J. Antony; S. Ehrlich; H. Krieg. A Consistent and Accurate Ab Initio Parametrization of Density Functional Dispersion Correction (DFT-D) for the 94 Elements H-Pu. *J. Chem. Phys.* **2010**, *132* (15), 154104. DOI: 10.1063/1.3382344.
36. G. Henkelman; B. P. Uberuaga; H. Jonsson. A Climbing Image Nudged Elastic Band Method for Finding Saddle Points and Minimum Energy Paths. *J. Chem. Phys.* **2000**, *113*, 9901-9904.
37. G. Mills; H. Jonsson; G. K. Schenter. Reversible Work Transition-state Theory - Application to Dissociative Adsorption of Hydrogen. *Surf. Sci.* **1995**, *324*, 305-337.

38. R. Grybos; L. Benco; T. Bučko; J. Hafner. Molecular Adsorption and Metal-support Interaction for Transition-metal Clusters in Zeolites: NO Adsorption on Pd_n (n=1–6) Clusters in Mordenite. *J. Chem. Phys.* **2009**, *130* (10), 104503. DOI: 10.1063/1.3079542.
39. G. Psofogiannakis; A. St-Amant; M. Ternan. Methane Oxidation Mechanism on Pt(111): a Cluster Model DFT Study. *J. Phys. Chem. B* **2006**, *110* (48), 24593-24605. DOI: 10.1021/jp061559+.
40. M. Chen; J. Li; W. Xue; S. Wang; J. Han; Y. Wei; D. Mei; Y. Li; J. Yu. Unveiling Secondary-Ion-Promoted Catalytic Properties of Cu-SSZ-13 Zeolites for Selective Catalytic Reduction of NOx. *J. Am. Chem. Soc.* **2022**, *144* (28), 12816-12824. DOI: 10.1021/jacs.2c03877.
41. W. Xue; D. Mei**.** Mechanistic understanding of methane combustion over H-SSZ-13 zeolite encapsulated palladium nanocluster catalysts. *Chem. Eng. J.* **2022**, *444*, 136671. DOI: 10.1016/j.cej.2022.136671.
42. J. Y. Luo; F. Gao; K. Kamasamudram; N. W. Currier; C. H. F. Peden; A. Yezerets. New insights into Cu/SSZ-13 SCR catalyst acidity. Part I: Nature of acidic sites probed by NH3 titration. *J Catal* **2017**, *348*, 291-299. DOI: 10.1016/j.jcat.2017.02.025.
43. M. Nielsen; R. Y. Brogaard; H. Falsig; P. Beato; O. Swang; S. Svelle. Kinetics of Zeolite Dealumination: Insights from H-SSZ-13. *ACS catal.* **2015**, *5*, 7131-7139. DOI: 10.1021/acscatal.5b01496.
44. Y. Cui; Y. Wang; D. Mei; E. D. Walter; N. M. Washton; J. D. Holladay; W. Wang; J. Szanyi; C. H. F. Peden; F. Gao. Revisiting Effects of Alkali Metal and Alkaline Earth Co-cation Additives to Cu/SSZ-13 Selective Catalytic Reduction Catalysts. *J. Catal.* **2019**, *378*, 363-375.
45. J. Song; Y. L. Wang; E. D. Walter; N. M. Washton; D. Mei; L. Kovarik; M. H. Engelhard; S. Prodinger; Y. Wang; C. H. F. Peden; et al. Toward Rational Design of Cu/SSZ-13 Selective Catalytic Reduction Catalysts: Implications from Atomic-level Understanding of Hydrothermal Stability. *ACS Catal.* **2017**, *7*, 8214-8227.
46. F. Gao; D. Mei; Y. Wang; J. Szanyi; C. H. F. Peden. Selective Catalytic Reduction over Cu/SSZ-13: Linking Homo- and Heterogeneous Catalysis. *J. Am. Chem. Soc.* **2017**, *139* (13), 4935-4942. DOI: 10.1021/jacs.7b01128.
47. C. B. Jones; I. Khurana; S. H. Krishna; A. J. Shih; W. N. Delgass; J. T. Miller; F. H. Ribeiro; W. F. Schneider; R. Gounder. Effects of dioxygen pressure on rates of NOx selective catalytic reduction with NH3 on Cu-CHA zeolites. *J Catal* **2020**, *389*, 140-149. DOI: 10.1016/j.jcat.2020.05.022.
48. C. Paolucci; A. A. Parekh; I. Khurana; J. R. Di Iorio; H. Li; J. D. A. Caballero; A. J. Shih; T. Anggara; W. N. Delgass; J. T. Miller; et al. Catalysis in a Cage: Condition-Dependent Speciation and Dynamics of Exchanged Cu Cations in SSZ-13 Zeolites. *J Am Chem Soc* **2016**, *138* (18), 6028-6048. DOI: 10.1021/jacs.6b02651.
49. J. H. Kwak; D. Tran; J. Szanyi; C. H. F. Peden; J. H. Lee. The Effect of Copper Loading on the Selective Catalytic Reduction of Nitric Oxide by Ammonia Over Cu-SSZ-13. *Catal Lett* **2012**, *142* (3), 295-301. DOI: DOI 10.1007/s10562-012-0771-y.
50. T. Zhang; H. Z. Chang; Y. C. You; C. N. Shi; J. H. Li. Excellent Activity and Selectivity of One-Pot Synthesized Cu SSZ-13 Catalyst in the Selective Catalytic Oxidation of Ammonia to Nitrogen. *Environ Sci Technol* **2018**, *52* (8), 4802-4808. DOI: 10.1021/acs.est.8b00267.
51. F. Gao; D. H. Mei; Y. L. Wang; J. Szanyi; C. H. F. Peden. Selective Catalytic Reduction over Cu/SSZ-13: Linking Homo- and Heterogeneous Catalysis. *J Am Chem Soc* **2017**, *139* (13), 4935-4942. DOI: 10.1021/jacs.7b01128.
52. J. S. McEwen; T. Anggara; W. F. Schneider; V. F. Kispersky; J. T. Miller; W. N. Delgass; F. H. Ribeiro. Integrated operando X-ray absorption and DFT characterization of Cu-SSZ-13 exchange sites during the selective catalytic reduction of NOx with NH3. *Catal Today* **2012**, *184* (1), 129-144. DOI: DOI 10.1016/j.cattod.2011.11.037.

53. V. Babrauskas; D. Leggett. Thermal decomposition of ammonium nitrate. *Fire Mater* **2020**, *44* (2), 250-268. DOI: 10.1002/fam.2797.
54. Y. Feng; T. V. W. Janssens; P. N. R. Vennestrøm; J. Jansson; M. Skoglundh; H. Grönbeck. The Role of H+- and Cu+-Sites for N2O Formation during NH3-SCR over Cu-CHA. *The Journal of Physical Chemistry C* **2021**, *125* (8), 4595-4601. DOI: 10.1021/acs.jpcc.0c11008.
55. J. Sun; Z. Sun; Q. Wang; H. Ding; T. Wang; C. Jiang. Catalytic effects of inorganic acids on the decomposition of ammonium nitrate. *Journal of Hazardous Materials* **2005**, *127* (1), 204-210. DOI: https://doi.org/10.1016/j.jhazmat.2005.07.028.
56. B. J. Wood; H. Wise. Acid Catalysis in the Thermal Decomposition of Ammonium Nitrate. *The Journal of Chemical Physics* **1955**, *23* (4), 693-696. DOI: 10.1063/1.1742078 (acccessed 2022/02/23).
57. J. J. Xue; X. Q. Wang; G. S. Qi; J. Wang; M. Q. She; W. Li. Characterization of copper species over Cu/SAPO-34 in selective catalytic reduction of NOx with ammonia: Relationships between active Cu sites and de-NOx performance at low temperature. *J Catal* **2013**, *297*, 56-64. DOI: DOI 10.1016/j.jcat.2012.09.020.
58. A. Y. Wang; Y. Chen; E. D. Walter; N. M. Washton; D. H. Mei; T. Varga; Y. L. Wang; J. Szanyi; Y. Wang; C. H. F. Peden; et al. Unraveling the mysterious failure of Cu/SAPO-34 selective catalytic reduction catalysts. *Nat Commun* **2019**, *10*, 1137. DOI: 10.1038/s41467-019-09021-3.
59. T. Selleri; F. Gramigni; I. Nova; E. Tronconi. NO oxidation on Fe- and Cu-zeolites mixed with BaO/Al2O3: Free oxidation regime and relevance for the NH3-SCR chemistry at low temperature. *Appl Catal B-Environ* **2018**, *225*, 324-331. DOI: 10.1016/j.apcatb.2017.11.068.
60. C. Negri; T. Selleri; E. Borfecchia; A. Martini; K. A. Lomachenko; T. V. W. Janssens; M. Cutini; S. Bordiga; G. Berlier. Structure and Reactivity of Oxygen-Bridged Diamino Dicopper(II) Complexes in Cu-Ion-Exchanged Chabazite Catalyst for NH3-Mediated Selective Catalytic Reduction. *J Am Chem Soc* **2020**, *142* (37), 15884-15896. DOI: 10.1021/jacs.0c06270.
61. C. Paolucci; I. Khurana; A. A. Parekh; S. C. Li; A. J. Shih; H. Li; J. R. Di Iorio; J. D. Albarracin-Caballero; A. Yezerets; J. T. Miller; et al. Dynamic multinuclear sites formed by mobilized copper ions in NOx selective catalytic reduction. *Science* **2017**, *357* (6354), 898-903. DOI: 10.1126/science.aan5630.
62. K. A. Lomachenko; E. Borfecchia; C. Negri; G. Berlier; C. Lamberti; P. Beato; H. Falsig; S. Bordiga. The Cu-CHA deNO(x) Catalyst in Action: Temperature-Dependent NH3-Assisted Selective Catalytic Reduction Monitored by Operando XAS and XES. *J Am Chem Soc* **2016**, *138* (37), 12025-12028. DOI: 10.1021/jacs.6b06809.
63. H. Kubota; C. Liu; T. Amada; K. Kon; T. Toyao; Z. Maeno; K. Ueda; A. Satsuma; N. Tsunoji; T. Sano; et al. In situ/operando spectroscopic studies on NH3-SCR reactions catalyzed by a phosphorus-modified Cu-CHA zeolite. *Catal Today* **2021**, *376*, 73-80. DOI: 10.1016/j.cattod.2020.07.084.
64. Y. N. Zhang; Y. Q. Wu; Y. Peng; J. H. Li; E. D. Walter; Y. Chen; N. M. Washton; J. Szanyi; Y. Wang; F. Gao. Quantitative Cu Counting Methodologies for Cu/SSZ-13 Selective Catalytic Reduction Catalysts by Electron Paramagnetic Resonance Spectroscopy. *J Phys Chem C* **2020**, *124* (51), 28061-28073. DOI: 10.1021/acs.jpcc.0c07971.
65. C. Negri; E. Borfecchia; M. Cutini; K. A. Lomachenko; T. V. W. Janssens; G. Berlier; S. Bordiga. Evidence of Mixed-Ligand Complexes in Cu-CHA by Reaction of Cu Nitrates with NO/NH3 at Low Temperature. *Chemcatchem* **2019**, *11* (16), 3828-3838. DOI: 10.1002/cctc.201900590.
66. A. Marberger; A. W. Petrov; P. Steiger; M. Elsener; O. Krocher; M. Nachtegaal; D. Ferri. Time-resolved copper speciation during selective catalytic reduction of NO on Cu-SSZ-13. *Nature Catalysis* **2018**, *1* (3), 221-227. DOI: 10.1038/s41929-018-0032-6.
67. C. Paolucci; A. A. Verma; S. A. Bates; V. F. Kispersky; J. T. Miller; R. Gounder; W. N. Delgass; F. H. Ribeiro; W. F. Schneider. Isolation of the Copper Redox Steps in the Standard Selective Catalytic

Reduction on Cu-SSZ-13. *Angew Chem Int Edit* **2014**, *53* (44), 11828-11833. DOI: DOI 10.1002/anie.201407030.

68. A. Godiksen; P. Vennestrom; S. Rasmussen; S. Mossin. Identification and Quantification of Copper Sites in Zeolites by Electron Paramagnetic Resonance Spectroscopy. *Top Catal* **2017**, *60* (1-2), 13-29. DOI: 10.1007/s11244-016-0731-7.
69. E. Fernandez; M. Moreno-Gonzalez; M. Moliner; T. Blasco; M. Boronat; A. Corma. Modeling of EPR Parameters for Cu(II): Application to the Selective Reduction of NOx Catalyzed by Cu-Zeolites. *Top Catal* **2018**, *61* (9-11), 810-832. DOI: 10.1007/s11244-018-0929-y.